**UNIVERSIDAD DE LAS AMÉRICAS PUEBLA**

**Escuela de Ciencias**

**Departamento de Ciencias Químico-Biológicas**

# ZIF-8/Nanocellulose-based composites for antibacterial applications in food packaging

Tesis que, para completar los requisitos del Programa de Honores presenta el estudiante

José Ángel Cuellar Sánchez

ID: 170831

Licenciatura en Nanotecnología e Ingeniería Molecular

Director de Tesis: Dr. Ricardo Navarro Amador

San Andrés Cholula, Puebla Otoño 2024

Hoja de firmas

Tesis que, para completar los requisitos del Programa de Honores presenta el estudiante José Ángel Cuellar Sánchez ID: 170831

**Director de Tesis**

_____

Dr. Ricardo Navarro Amador

**Presidente de Tesis**

_____

Dra. Jessica Rosaura Campos Delgado

**Secretario de Tesis**

_____

Dra. Mónica Cerro López

**Agradecimientos**

A mi familia, a mis profesores, a mis amigos, a mi novia Anna y a todos aquellos con los que crucé camino a lo largo de estos últimos años. Gracias por hacer del viaje tan divertido, interesante y llenador como el destino mismo.

**Table of Contents**

## Introduction

Food insecurity (commonly designated as hunger or famine) is perhaps one of the most challenging problems we face as a society, affecting around 800 million people in 2022. The Food and Agriculture Organization of the United Nations, FAO, designates food insecurity as "the lack of regular access to enough safe and nutritious food for normal growth and development and an active and healthy life". It can be classified as moderate or severe: moderate food insecurity is characterized by a reduced quality or quantity of food, leading to malnutrition-related health concerns: stunting, nutrient deficiencies or obesity in adults. Severe food insecurity entails a large period of time (days) without food (Food and Agriculture Organization of the United Nations, n.d.).

Data recovered by the World Food Programme reveals that famine is mostly present in eastern Africa (that is: Nigeria, Burkina Faso, Guinea, Sierra Leone, etc.) the Middle East (Turkey, Syria, Iran, Yemen, Afghanistan) and the Sub Indian continent, Pakistan and Bangladesh. In the Americas, insufficient food consumption is present in Haiti, followed by Jamaica and Cuba, Venezuela, Guatemala and the northernmost part of Colombia. To a lesser extent, Mexico presents moderately low food consumption spread across the center and south of the country (World Food Programme, n.d.).

Food insecurity is a deeply profound issue, with its causes including poverty, inequity, discrimination, deficient government and health institutions, etc. (Actions Against Hunger, n.d.). According to the *Consejo Nacional de Evaluación de la Política de Desarrollo Social* (CONEVAL), 55.7 million Mexicans suffer poverty, 10.8 million of them exhibiting extreme poverty (CONEVAL, n.d.). The geographical link between poverty and food insecurity is

further corroborated by reviewing the country´s highest poverty rates by state: Guerrero (75% poverty rate), Chiapas (74%), Puebla (66%) and Oaxaca (61%) (CONEVAL, n.d.).

Food waste is also a common phenomenon: data recovered by Greenpeace suggests that in Mexico 34.7% of all aliments got to waste or are thrown away. Of this amount, the most commonly discarded food is pork meat, followed by fish, beef, chicken and tortilla. Such losses occur throughout the entire life cycle of the products: during the harvesting phase weather phenomenons or human errors during handling might degrade the quality of the food. More than that, inadequate storage can reduce the shelf life of food or deteriorate its nutritional properties. Finally, in the transport process, food can be damaged due to poor packaging, lack of infrastructure or inadequate transport routes (Soto, 2020).

Food spoilage refers to the physical, chemical and biological processes that make them unfit for human consumption (Food and Agriculture Organization of the United Nations, n.d.). Deterioration might occur due to various factors, ranging from light and heat exposure, temperature, humidity or oxygen (Fung, 2009). Nonetheless, microbiological analysis stands as a quantitative way to predict the spoilage potential of food, as stated by Fung et al., 1980:

Table 1. Spoilage potential of foods as a function of CFU*. Based on data by (Fung et al, 1980)

| | **CFU Range** |
|---|---|
| Low count | $10^{0-2}$ |
| Intermediate count | $10^{3-4}$ |
| High count | $10^{5-6}$ |
| Spoilage initiation | $10^{7}$ |
| Odor development | $10^{8}$ |
| Slime development | $10^{9}$ |
| Unacceptable for human consumption | $10^{10}$ |

*CFU stands for colony-forming units per ml, $cm^2$ or g of food.

There have been many efforts to produce nanotechnology based antimicrobial food packaging, all of them based on the inclusion of an active material located in near proximity of the food. Some examples include (Sonawane et al., 2018):

- Chitosan matrix reinforced with ZnO nanoparticles, effective against E. Coli and C. Albicans
- Ag and TiO2 reinforced polymers with enhanced barrier and mechanical properties. The composite was noted to extend the shelf life of grapes by two weeks in comparison with traditional packaging.
- Polyethylene membranes doped with Ag or TiO2 nanoparticles stopped the growth of Aspergillus flavus even at high temperature and humidity.
- Polyethylene doped with calcium carbonate was observed to stop the fungal and bacterial growth in sweet potatoes.

An antimicrobial agent is a substance that can prevent the growth of microorganisms by disrupting necessary cellular metabolism steps, thus killing the organism and/or disrupting any further replication processes (Di Martino, 2022).

In the case of the antimicrobial agents used in the aforementioned composites (that is, metallic nanoparticles: Ag, ZnO, TiO2), their characteristics are further explained:

There is not a definitive mechanism responsible for the antimicrobial effect of silver nanoparticles, as different environmental conditions might interfere in the properties of the nanoparticles. It is theorized however that the constant release of $Ag^{+}$ ions disrupt the bacterial cell wall by electrostatically adhering to it and increasing permeability. The silver cations also deactivate the respiratory enzymes, triggering the production of reactive oxygen species that interrupt ATP release, hinder DNA replication and stop cell propagation (Anees et al., 2020; Bruna et al., 2021).

In the case of ZnO nanoparticles, similar mechanisms can be attributed, cell wall disruption, DNA binding and ROS generation (Gudkov et al., 2021; Mendes et al., 2022).

An alternative to the use of metallic nanoparticles is essential oils. In the present work eugenol is used. Eugenol is a primary component of various essential oils, commonly extracted via steam distillation of clove or cinnamon oil with over 95% purity. It can also be synthesized via the reaction of guaiacol with allyl chloride, however, poor yields make this route inconvenient (Wexler, 2014).

Similarly to ZnO or Ag nanoparticles, eugenol disrupts the bacterial membrane, prompting the release of ATP and other contents from within the cell, causing bacterial death (Jeyakumar & Lawrence, 2021).

The Nanocellulose-ZIF-Eugenol (NcZ) nanocomposite hereby presented supposes a cheaper way to synthesize antimicrobially active material for food packaging applications, as it requires easily affordable reagents coupled with low cost-low energy synthetic procedures. The aforementioned qualities also make the nanocomposite ecologically friendly, being simpler to produce than metal nanoparticle based active materials. Viewed from a health perspective, the NcZ composite stands as a less risky alternative, as it eliminates the possibility of ingesting metallic nanoparticles with serious implications in human health (Noga et al., 2023).

Hunger is a far-reaching problem, cross-cutting societal, economical and infrastructural deficiencies regarding how food is managed and distributed. And, as the world's population is predicted to hit 9.1 billion in the year 2050, food availability across the globe needs to grow 70% from today's value (Rezaei & Liu, 2017).

Herein, by introducing novel essential oil-based antimicrobial active food packaging, it is intended to prolong the shelf life of commonly discarded foods, thus effectively creating a new source of nourishment out of foods that would otherwise be wasted by providing food safe, stable and functional active packaging that preserves food on-route to impoverished areas. On a consumer and industry level, the introduction of this technology might suppose a way to extend the storage time supplies, make food distribution and transport safer, and provide the public the assurance that their product is fresh.

**Justification**

The current socioeconomic and political landscape has put considerable stress over the underdeveloped sectors of the population. Whilst specific threats have been addressed, challenges like hunger, undernourishment and food insecurity have plateaued substantially, with data suggesting undernourishment levels equal to those 15 years back (United Nations, 2024). Present and future challenges such as overpopulation, food waste and climate change further exacerbate the situation, accentuating the weaknesses in today's food distribution system and highlighting the necessity for new food packaging technologies.

In this thesis, a novel Nanocellulose-ZIF-Eugenol (NcZ) composite material is proposed as a means to increase the shelf life of commonly perishable foods by halting bacterial growth in the food package environment. The inclusion of this technology might create a pathway for food that would otherwise be wasted to be consumed and benefited from. More than that, the NcZ composite might find applications in all of the food production process steps, from initial storage after harvesting to transportation.

## General Objectives

Fabricate composite materials based on ZIF-8 embedded nanocellulose fibrils and their subsequent functionalization using eugenol essential oil. Gauge the composite's antimicrobial efficacy via well diffusion assays.

## Specific Objectives

- Synthesize crystalline, high yield ZIF-8 via a green chemistry-adjacent synthetic method
- Successfully incorporate ZIF-8 into a nanocellulose matrix
- Examine the generated composite's antimicrobial activity

## Literature Review

Metal organic frameworks, commonly abbreviated as MOFs, designate a family of solid materials characterized by high porosity, high specific surface areas and great thermal stability. According to the classification by IUPAC in 2013, MOFs are catalogued as a sub-class of coordination networks, which in turn are a sub-class of coordination polymers (Raptopoulou, 2021). Since their conception, more than 90,000 types of MOFs have been reported (Yusuf et al., 2022).

Metal organic frameworks are created via the coordination complexation of metal ion nodes and organic ligands, which can form periodic networks spanning in one, two or three dimensions. In said interaction, the ligands (oftentimes containing donor species like N, B, F) bind to the metallic cation by a coordinate covalent bond, forming a secondary building unit (SBU), whose geometry (that is, coordination geometry) is decided by the node and ligand used. The aforementioned physical characteristics of MOFs such as crystallinity,

topology, porosity and thermal stability are heavily dependent on the SBU (Raptopoulou, 2021), thus enabling a fine tuning of the materials attributes.

There are many synthetic routes by which the creation of metal organic frameworks is achieved. Here are included the most commonly used methods (Claudio-Rizo, et al., 2021):

- Solvothermal: Characterized by the dilution of metallic salts and the ligands in organic solvents (hydrothermal would be the appropriate term if water was used). The solution is transferred into a Teflon liner and into a stainless-steel autoclave, which then undergoes high temperatures (causing high pressures inside the container) for large periods of time. Such methodologies are known to be simple, convenient and high yield with good crystallinity.
- Electrochemical: Unlike the solvothermal method, the source of metal ions is an electrode which is placed inside a solution containing the dissolved ligands. By applying a determined voltage, the ions are liberated onto the solution, forming MOFs near the electrode surface.
- Mechanochemical: In this method, a mixture of metal salts and ligands in the solid state is ground, exposed to heat to evaporate volatile and dry. The MOF is created via the mechanical bond breaking of the original species. It is characterized by batch sizes and simple reaction conditions.
- Microwave assisted: Similarly to solvothermal methods, a mixture of ligands and metal salts dissolved in an organic medium is placed in a sealed Teflon container. The container is microwaved at an appropriate frequency for as long as 24 hours or more. Uniform sized MOF nanocrystals are produced.

In each case, the resulting framework is highly stable due to the intramolecular and intermolecular forces and interactions between different chemical species, coupled with more complex structural geometries (squares and octahedra, for example). The strong covalent bonds present in most types of MOFs (C-C, C-H, C-O and M-O) also give them excellent thermal stability, ranging from couple hundred degrees centigrade up to 500°C (Furukawa et al., 2013).

The ZIF family of metal organic frameworks consist of a zeolite-like framework of Co or Zn metallic nodes tetrahedrally coordinated via imidazole ligands. It was first reported in 2006 (Zen et al., 2021; Elaouni et al., 2022). Its most studied member is ZIF-8, commonly synthesized using 2-methylimidazole ligands and Zn (II) nodes (Zeng et al., 2021) like that of zinc nitrate hexahydrate. It owes its popularity due to high thermal and chemical stability, high loading capacity, big pore size, adsorption capacity and functional site tuning. It is typically synthesized hydro/solvothermically (Claudio-Rizo, et al., 2021).

Cellulose is the most abundant organic material on earth (American Chemical Society, n.d.), a primary component of plants, algae and bacteria. Because of this, cellulose is highly renewable, as well as biodegradable and biocompatible (Manoukian et al., 2019). The aforementioned qualities, alongside attainable prices, have made cellulose a sought-after material in various fields of study. The fabrication process of nanocellulose starts with a purification step of the raw material. Physical and chemical processes aim to remove impurities from the cellulose, and consist in the removal of undesirable materials like lignin, hemicellulose, tannins, sugar, etc. The secondary step removes amorphous domains of cellulose, leaving behind pristine, crystalline structures (Trache et al., 2020). The properties of nanocellulose include high mechanical strength, low density, high flexibility, chemical

inertness, thermal stability, high surface modification and high surface area (Kaur et al., 2021; Kargarzadeh et al., 2018).

Further preparation treatments yield different types of nanocellulose, two of them being of major importance: cellulose nanocrystals (CNCs) and cellulose nanofibrils (CNFs). As stated by their name, CNCs are polyhedral nanoparticles with few nanometers in diameter and lengths of 10-500 nm. CNFs on the other hand are wirelike structures with diameters in the range of 3-50 nm and lengths up to micrometers (Kargarzadeh et al., 2018).

A composite material refers to an assembly of two or more materials which combine to form a final product of increased qualities over the original substances: a mixture of advantages provided by each starting material. Such improvements might include better strength, stiffness, increased resistance to wear, corrosion and fatigue among other mechanical properties (Carey, 2017). The fabrication process of basic composites has been known for thousands of years, (Carey, 2017) nonetheless, advanced composite materials, the current epitome of high technology - highly specialized materials can be roughly traced back to the 1940s, amid military and aerospace development (Linganiso et al., 2016).

On a more specialized manner, for a material to classify as a nanocomposite, it must contain at least one phase in the nanoscale range (typically from 1-3 nm) (Shahbaz et al., 2024). In this case, the continuous phase, the matrix, is reinforced by a nano-sized discontinuous phase, which may be composed of a variety of nanomaterials or nanostructures.

ZIF-8/cellulose composite systems have had interesting ventures in the biomedical and food sector: Di Matteo et al., 2023 studied the antibacterial properties of ZIF-8 functionalized cellulose fibers in wound dressings. The system proved effective bactericidal

properties against Gram-positive and Gram-negative strains, while being innocuous to the Hel 299 cell line used as model mammalian cells (Di Matteo et al., 2023).

Another ZIF/bacterial nanocellulose composite material was developed by Molaei et al., 2022 as a food freshness sensor. Similarly, cellulose and ZIF-8 composites were generated, and grape anthocyanins were used to functionalize the system, exhibiting a colorimetric response to food rot, particularly minced meat and shrimp (Molaei et al., 2022).

As mentioned in the previous section, the composite material generated in this work uses a nanocellulose fibril matrix embedded with ZIF-8 and doped with eugenol. The ZIF/cellulose composition exhibits remarkable antimicrobial capabilities, which will be further studied by the addition of eugenol and a more rigorous insight into the material science behind the composite's fabrication procedure.

## Methodology

### Reagents and Equipment

Zinc nitrate hexahydrate ($Zn(NO_3)_2*6H_2O$) was purchased from *Reactivos Fermont* and 2 methylimidazole ($CH_3C_3H_2N_2H$) was acquired from Sigma Aldrich. Carboxymethyl cellulose in the powder form was purchased from *Reactivos Meyer*. Scanning Electron Microcopy (SEM) was carried out by a Tescan MAIA 3 Triglav coupled with a Bruker XFlash 630 Detector for Energy dispersive X-ray (EDX) spectroscopic analysis. Fourier Transform Infrared (FTIR) spectroscopy was executed by an Agilent Technologies Cary 630 spectrometer with an Attenuated Total Reflectance (ATR) module. Finally, Raman analysis was carried out in a Horiba XploRA PLUS confocal Raman microscope using a laser with wavelength of 532 nm.

### Synthesis of zeolitic imidazolate framework (ZIF-8)

The fabrication of ZIF-8 was approached with the paramount objective of achieving a high crystallinity material via a time effective, non-specialized synthetic route that involved nontoxic solvents as well as produced the minimum amount of chemical waste possible. Because of this, common synthetic routes such as solvothermal and mechanochemical methods (Lee et al., 2015) were avoided. Thus, an aqueous synthesis method carried out at room pressure was adopted to carry out the fabrication of ZIF-8.

To evaluate the effects of nucleation temperature and cation:ligand ratio on the physical and chemical characteristics of the resulting MOF, the ZIF-8 was synthesized at various temperatures and various metal salt and ligand concentrations. Namely, two synthetic routes were taken: the first one carried out at room temperature with cation:ligand ratios of

1:2 and 1:8. The second synthetic route was carried at high temperatures (75°C) with a cation:ligand ratio of 1:55.

The room temperature ZIF-8 (rtZIF-8) was prepared based on a modified procedure by (Zhang, 2018). For the 1:2 molar ratio, 1.17 g of zinc nitrate hexahydrate ($Zn(NO_3)_2*6H_2O$) and 0.65 g of 2 methylimidazole (Hmim) were each suspended in 6.5 g of water and thoroughly dissolved. After complete dissolution, the zinc nitrate solution was slowly added into the Hmim solution. A coloration change from translucent to cloudy white signified the formation of ZIF-8 crystals. After stirring for a couple of minutes to ensure the complete nucleation and growth of the ZIF-8, the product was washed with distilled water and centrifuged in triplicate before doing a solvent exchange with ethanol and repeating the washing process. The cleaned product was dried at room temperature and pressure for 72 hours. For the 1:8 molar ratio, the mass amount of zinc nitrate hexahydrate remained the same at 1.17 g, while 2.62 g of Hmim were used. The synthetic, washing and drying procedures remained the same.

The ZIF-8 synthesis at high temperatures (htZIF-8) was carried in accordance with a procedure by (Lestari, 2012) with some modifications: 0.29 g of zinc nitrate hexahydrate was dissolved in 10 ml of distilled water while 4.54 g of Hmim was dissolved in 15 ml of distilled water. Both solutions were taken up to a temperature of 75°C for 30 minutes under vigorous stirring. Consequently, the zinc nitrate solution was slowly added to the Hmim solution. The ZIF-8 formation was accompanied by an instantaneous change in color to a deep white. The temperature of 75°C was sustained for 10 minutes before lowering it to 40°C and letting the reaction solution stir for an hour. After that, the product was washed and dried according to the aforementioned steps. Table 1 summarizes the synthesized MOFs:

Table 2. Synthesized ZIF-8 variations

| Composite | Zinc nitrate hexahydrate | Hmim | Cation:ligand ratio |
|---|---|---|---|
| rtZIF-8 1 | 1.17 g | 0.65g | 1:2 |
| rtZIF-8 2 | 1.17 g | 2.62 g | 1:8 |
| htZIF-8 | 0.29 g | 4.54 g | 1:55 |

**Synthesis of the nanocellulose-ZIF8 composite (NcZ composite)**

The composite fabrication was carried out *in situ* by the addition of the matrix material to the ZIF-8 reaction mixture. In accordance with the htZIF-8 synthesis, 0.444 g of carboxymethylcelluose (CMC) was slowly added to the Hmim solution during the initial heating process; the elevated temperatures ensured a full dissolution of the cellulose into distilled water. Having stabilized the Hmim-CMC mixture temperature to 75°C, the zinc nitrate hexahydrate solution was added slowly, once again resulting in a color change from translucent to deep white. The resulting composite was subjected to 3 cycles of washing and centrifuging with water before repeating the process with ethanol. The majority of the solvent was removed, and the samples were placed in a freezer for up to 24 hours prior to the freeze-drying process.

In order to examine the loading effect of the ZIF-8 over the CMC matrix, NcZ composites with different loading percentages of MOF were synthesized, as summarized in the following Table:

Table 3. Synthesized NcZ composite variations.

| Composite | Zinc nitrate hexahydrate | Hmim | Theoretical ZIF-8 weight * | CMC | ZIF-8 Loading percentage |
|---|---|---|---|---|---|
| NcZ1 | 0.29 g | 4.54 g | 0.223 g | 0.444 g | 50% |
| NcZ2 | 0.145 g | 2.27 g | 0.111 g | | 25% |
| NcZ3 | 0.0725 g | 1.135 g | 0.055 g | | 12.5% |
| NcZ4 | 0.03625 g | 0.567 g | 0.0275 g | | 6.25% |

*Note: For a comprehensive summary of the theoretical and experimental yields of htZIF-8, please reference the Results section.

To gauge the effect of the composite's humidity before freeze drying, both humid and dry composites were lyophilized and their physical characteristics analyzed. Humid composites refer to materials where most of the solvent was removed prior to the freezing step, however, no drying efforts were made. Dry composites refer to materials actively dried (at room temperature) before freezing.

**Functionalization of the NcZ composites with eugenol**

The impregnation of the NcZ composites with eugenol, as well as the antimicrobial activity analyses, were carried out by Rosa Hernández of the Department of Chemical, Food and Environmental Engineering, UDLAP. In brief, the generated composites were suspended in water and stirred constantly at 50°C for 20 minutes. After that, eugenol (0.1, 0.5, 1% v/v) was added to the mixture and further stirred. This eugenol-NcZ (E-NcZ) mixture was used in the subsequent antimicrobial assays.

**Antimicrobial activity**

The composite's antimicrobial activity was evaluated using a well-diffusion inhibition zone test in an inoculated agar plate containing *Staphylococcus aureus* (*S. aureus*). The growth medium was punched to form 5 holes of 9 mm in diameter, with each hole being filled with the E-NcZ mixture. The petri dishes were sealed and placed in an incubator at 37°C for 24 hours. The antimicrobial performance was evaluated as a function of the inhibition zone diameter around the well (the assay was carried out in triplicate).

## Results and Discussion

### rtZIF-8

### rtZIF-8 1 yield

When utilizing zinc nitrate hexahydrate and Hmim as precursors, the formation of ZIF-8 occurs as displayed in the equation below:

$$Zn(NO_3)_2 \cdot 6H_2O + 2C_4H_6N_2 \rightarrow Zn(C_4H_5N_2)_2 + 2HNO_3 + 6H_2O$$

As previously stated, the synthesis of rtZIF-8 1 was carried out with 1.17 g of zinc nitrate and 0.65 g of Hmim for a molar ratio of 1:2. Calculating the mol amount for each reactant:

$$1.17\ g\ Zn(NO_3)_2 \cdot 6H_2O = \left(\frac{1\ mol}{297.49\ g}\right) = 3.932\ x10^{-3}\ mol = 3.932\ mmol$$

$$0.65\ g\ 2C_4H_6N_2 = \left(\frac{1\ mol}{82.10\ g}\right) = 7.917x10^{-3}\ mol = 7.917\ mmol$$

As expected, the zinc nitrate hexahydrate acts as the limiting reactant for the production of ZIF-8. Proceeding with the calculation of the theoretical yield for the weight amount of reactants used:

$$3.932\ x10^{-3}\ mol\ Zn(NO_3)_2 \cdot 6H_2O = \left(\frac{1\ mol\ ZIF-8}{1\ mol\ Zn(NO_3)_2 \cdot 6H_2O}\right)$$

$$= 3.932\ x10^{-3}\ mol\ ZIF-8$$

$$3.932\ x10^{-3}\ mol\ ZIF-8 = \left(\frac{229.6\ g}{1\ mol\ ZIF-8}\right) = 0.902\ g\ ZIF-8$$

The synthesized rtZIF-8 1 was recorded at a weight of 0.0525 g, giving way to the determination of the experimental yield:

$$Experimenal\ yield = \frac{0.0525\ g}{0.902\ g} * 100 = 5.82\ \%$$

**rtZIF-8 2 yield**

In the rtZIF-8 2 synthesis the molar ratio was increased towards Hmim at a final 1:8 proportion, equaling an increment in mass for the Hmim from 0.65 g to 2.62 g while the quantity of zinc nitrate remained consistent. On this basis, the theoretical yield for the ZIF-8 remained the same:

$$3.932\ x10^{-3}\ mol\ ZIF-8 = \left(\frac{229.6\ g}{1\ mol\ ZIF-8}\right) = 0.902\ g\ ZIF-8$$

The rtZIF-8 2 material weighted at 0.6435 g, thus giving the following experimental yield for the material:

$$Experimenal\ yield = \frac{0.6435\ g}{0.902\ g} * 100 = 71.43\ \%$$

As expected, a larger amount of Hmim promptly facilitated the formation of ZIF by introducing an excess of ligand to the reaction environment. This effect in the yield can be seen macroscopically by comparing the reaction mixture of both 1:2 and 1:8 molar ratios:

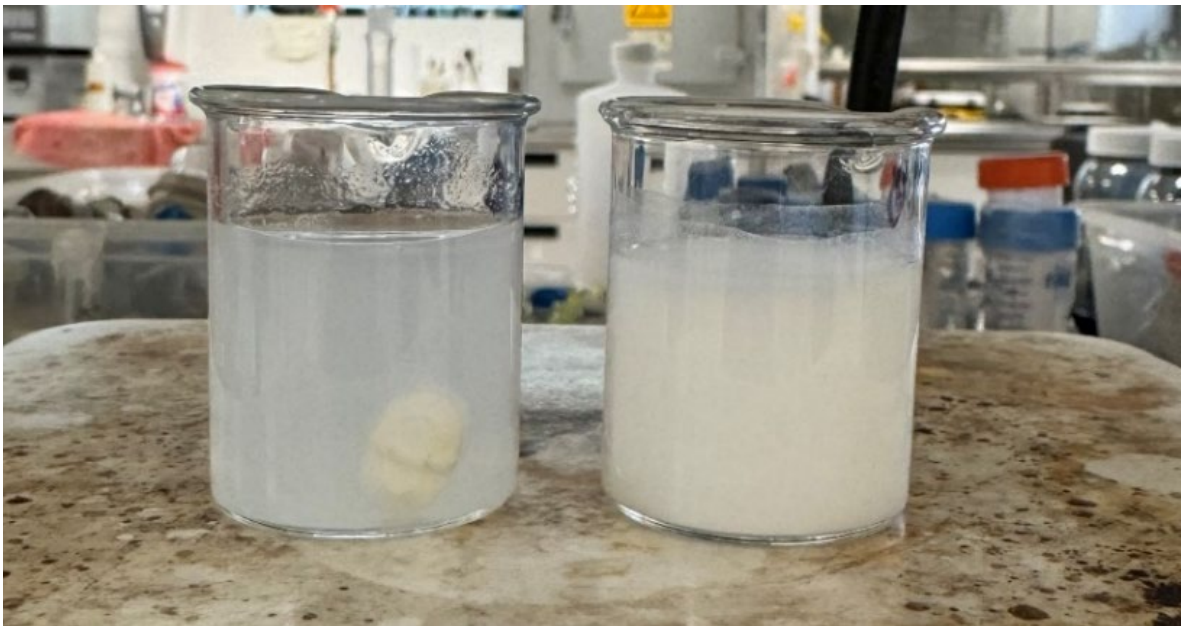

Figure 1. Left: rtZIF-8 6t1 reaction mixture. Right: rtZIF-8 2 reaction mixture.

Note that the lefthand side beaker, containing the rtZIF-8 1, appears much clearer in comparison with the solid white color of the rtZIF-8 2 reaction mixture. This acts as a qualitative indicator that confirms that a much lesser amount of ZIF-8 crystals were formed by the 1:2 molar ratio in comparison with its 1:8 counterpart.

**rtZIF-8 XRD and SEM Characterization**

The XRD spectra recovered for the room temperature ZIF-8 (rtZIF-8 1 and rtZIF-8 2) are shown below:

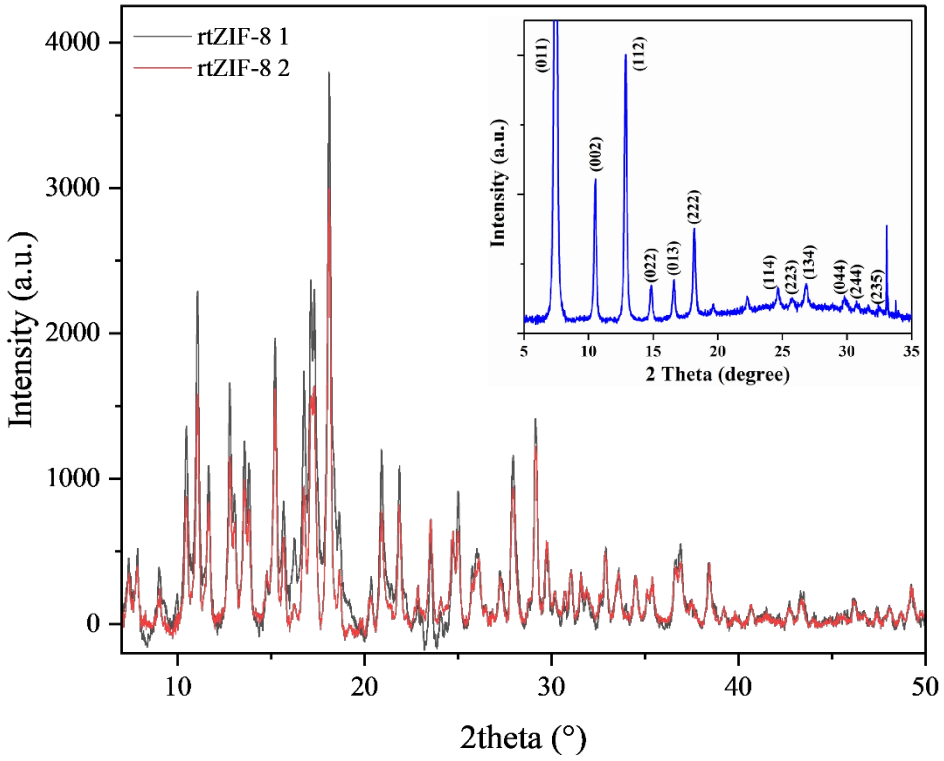


Figure 2. XRD spectra for the rtZIF-8 1 and 2 samples. Insert: XRD spectrum for ZIF-8 (Chappanda et al., 2018).

Both rtZIF-8s present poor crystallinity, as indicated by the lack of distinctive sodalite peaks in comparison with the insert from the literature (most notably the six distinct peaks between 5° and 20°, corresponding to the (011), (002), (112), (022), (013) and (222) crystallographic planes). The most notable band for both materials appears at roughly 18°, with an intensity almost three times that of the median peak. This correlates with the peaks of Hmim:

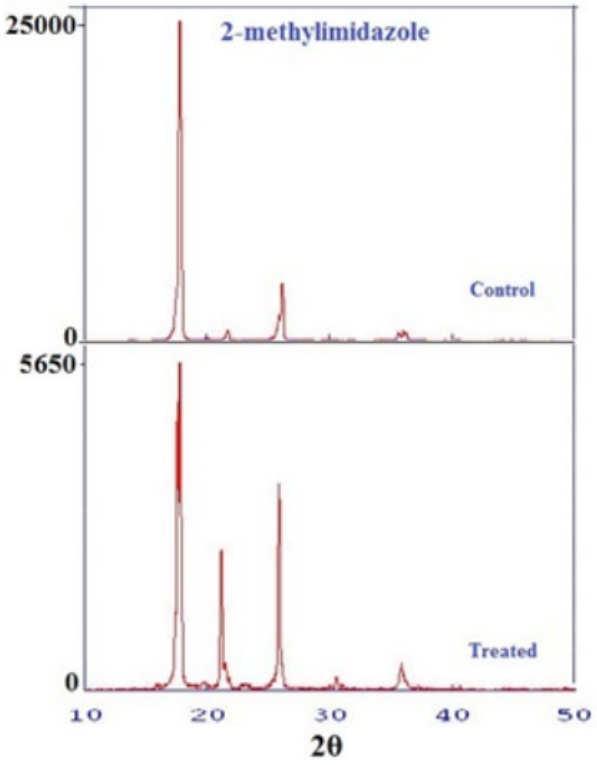


Figure 3. XRD Spectra of Hmim (Trivedi et al., 2015).

The Hmim peaks present in the rtZIF-8 samples suggest that a considerable amount of ligand did not bind with the metallic salt to form ZIF-8 crystals. This lack of crystallinity at low temperatures and low Zn:Hmim ratio is in accordance with observations by Malekmohammadi et al., 2019. It is theorized that the low cation:ligand ratio coupled with low temperature and ambient pressure could not propitiate nucleation in a crystalline manner, explaining the various peaks observed throughout the XRD spectra (Malekmohammadi, et al., 2019).

This fact is corroborated by examining the SEM micrographs of each material. Figure 4 compiles the morphology observed for the rtZIF-8 1 material:

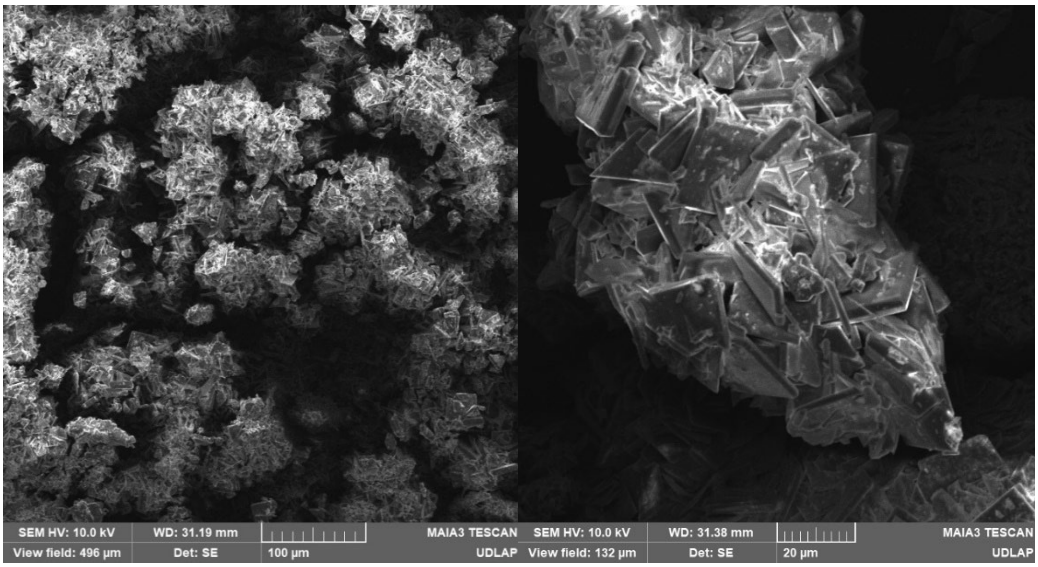


Figure 4. SEM micrographs for the rtZIF-8 1 material.

Note the overwhelming heterogeneity in crystal size and shape, rightfully explaining the XRD behavior observed previously. As seen by the left-hand side micrograph, the material is agglomerated into tight bundles, which in turn are composed of semi-amorphous ZIF-8 crystals of rectangular prism-like morphologies of up to 20 µm in length. In contrast, the literature for 1:2 ZIF-8 reports a truncated dodecahedron morphology:

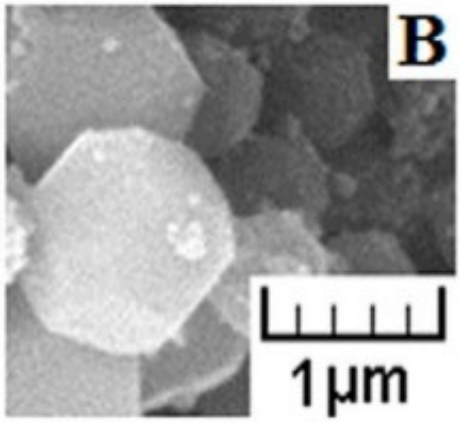


Figure 5. Typical truncated dodecahedron morphology of ZIF-8 (Zhang et al., 2018).

Examining the rtZIF-8 2 MOF:

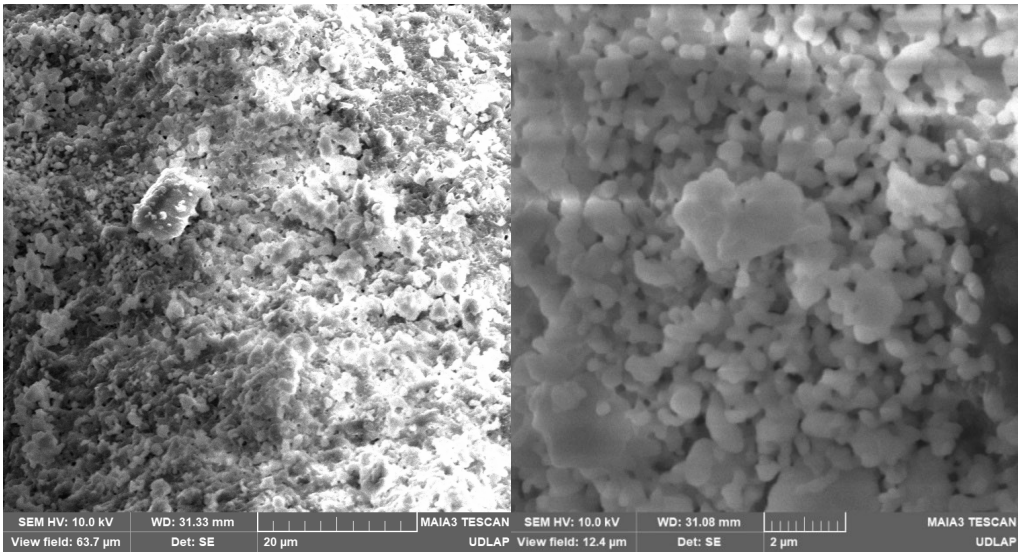


Figure 6. SEM micrographs for the rtZIF-8 2 material.

In comparison with the previous material, the ZIF-8 crystal size is notoriously smaller, averaging a diameter of around 0.25 µm. The morphology of the crystals more closely resembles that of the desired truncated rhombic dodecahedra, nevertheless, the homogeneity both in terms of shape and size leaves to be desired. The reduction in crystal size for the 1:8 ZIF-8 can be partially attributed to the fact that the abundance of Hmim completely engulfs the Zn cations, slowing down particle growth and hindering the final size of the crystals (Yamamoto et al., 2013).

**htZIF-8**

**htZIF-8 yield**

Once again, the calculation of the theoretical and experimental yield is done in accordance with the equation previously introduced for the formation of ZIF-8:

$$Zn(NO_3)_2 \cdot 6H_2O + 2C_4H_6N_2 \rightarrow Zn(C_4H_5N_2)_2 + 2HNO_3 + 6H_2O$$

Calculating the mol amount for each reactant, recall that 0.29 g of zinc nitrate were reacted with 4.54 g of Hmim for a 1:55 molar ratio:

$$0.29\ g\ Zn(NO_3)_2 \cdot 6H_2O = \left(\frac{1\ mol}{297.49\ g}\right) = 9.748\ x10^{-4}\ mol = 0.9748\ mmol$$

$$4.54\ g\ 2C_4H_6N_2 = \left(\frac{1\ mol}{82.10\ g}\right) = 0.0552\ mol = 55.2\ mmol$$

Proceeding with the calculation of the theoretical yield for the weight amount of reactants used:

$$9.748\ x10^{-4}\ mol\ Zn(NO_3)_2 \cdot 6H_2O = \left(\frac{1\ mol\ ZIF-8}{1\ mol\ Zn(NO_3)_2 \cdot 6H_2O}\right)$$

$$= 9.748\ x10^{-4}\ mol\ ZIF-8$$

$$9.748\ x10^{-4}\ mol\ ZIF-8 = \left(\frac{229.6\ g}{1\ mol\ ZIF-8}\right) = 0.2238\ g\ ZIF-8$$

For the htZIF-8 synthesis, the final weight of the product was recorded at 0.223 g, as seen in the following Figure:

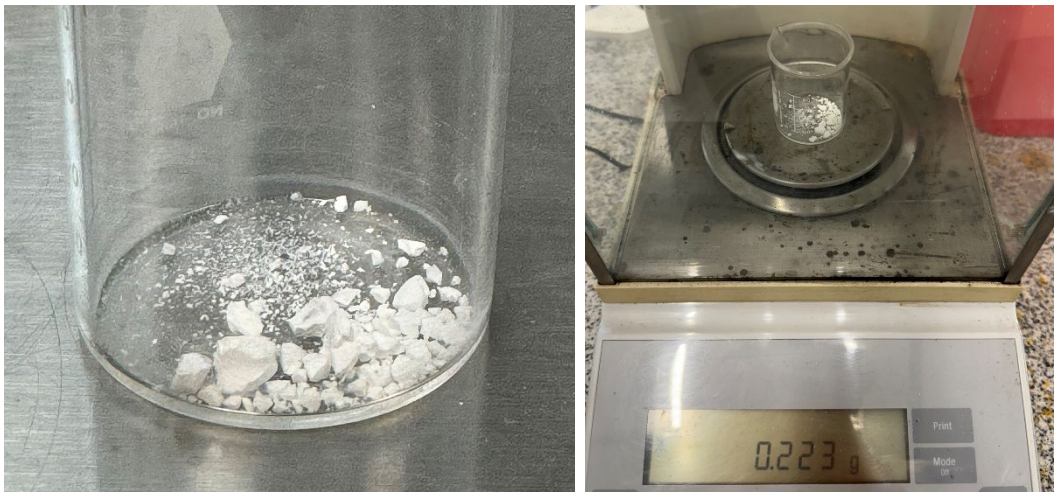


Figure 7. Recovered weight for the htZIF-8 synthesis

Thus, calculating the experimental yield:

$$Experimenal\ yield = \frac{0.223\ g}{0.2238\ g} * 100 = 99.64\%$$

It is not uncommon for aqueous synthesis of ZIF-8 to have yields over 97%, however, in some cases a part of this mass is attributed to the formation of various compounds aside of the desired ZIF-8, such as zinc hydroxide nitrate ($Zn_5(OH)_8(NO_3)_2{\cdot}2H_2O$) and the presence of unreacted ligand trapped in the cavities of the metal organic framework (Kida et al., 2013), especially when working with such high cation:ligand ratios. The latter hypotheses are disproven via XRD characterization (see the following section).

**htZIF-8 XRD and SEM Characterization**

The XRD spectrum for the high temperature ZIF-8 is attached:

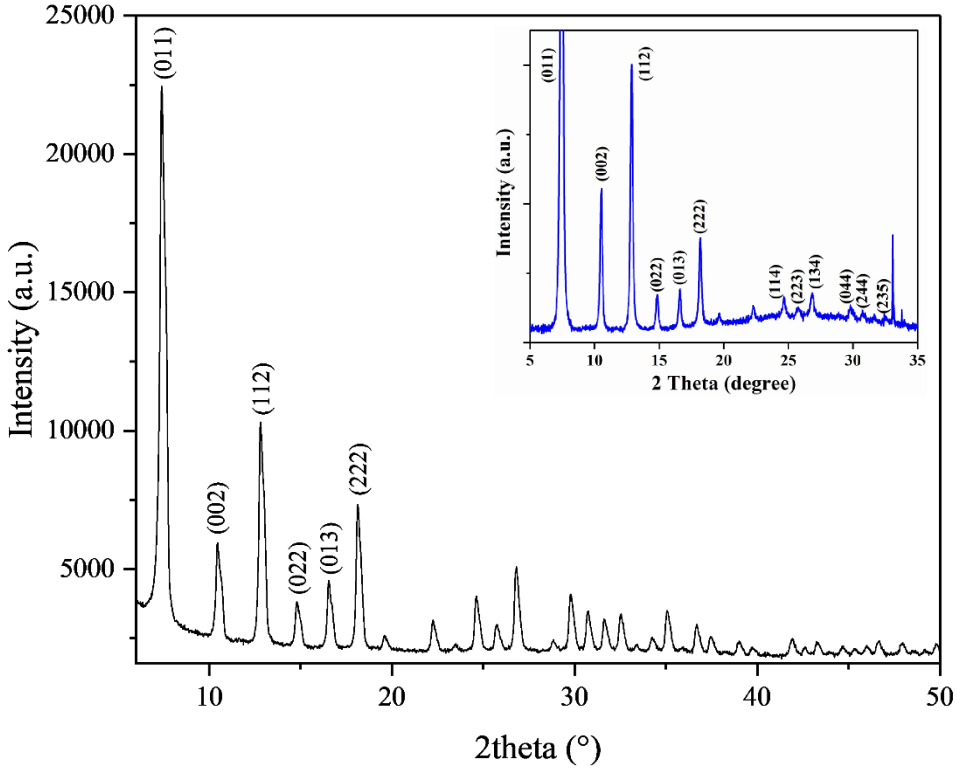


Figure 8. XRD spectrum for the htZIF-8 material. Insert: XRD spectrum for ZIF-8 (Chappanda et al., 2018).

A clear match between the recovered diffractogram and the literature can be observed: the htZIF-8 presents the six typical sodalite peaks below 20°, synonymous with high crystallinity. Notably, although a high Zn:Hmim was used, no foreign peaks can be observed, ruling out the presence of unreacted ligand or zinc hydroxide nitrate ($Zn_5(OH)_8(NO_3)_2 \cdot 2H_2O$). This synthetic route proved to be a reliable way of producing highly crystalline ZIF-8, as seen in Figure 8. Notice that for all synthesized samples the position and relative intensity of every sodalite peak is conserved and in good agreement with the literature:

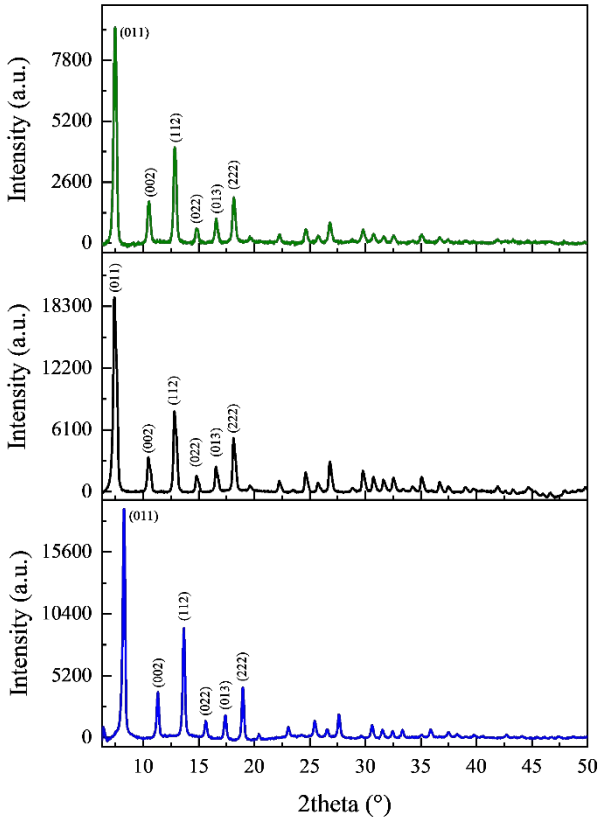


Figure 9. XRD spectra of various synthesized htZIF-8 samples.

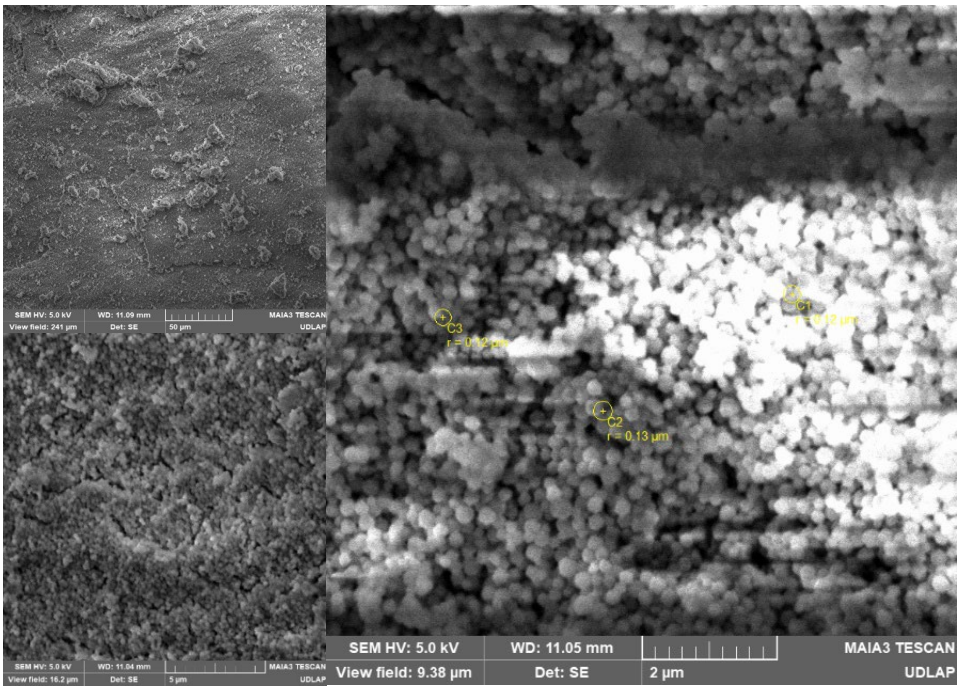


Figure 10. SEM micrographs for the htZIF-8 material.

Figure 10 shows the SEM micrographs recovered for the htZIF-8 material. As can be seen, htZIF-8 is composed of highly monodispersed crystals of diameters around 0.1 μm. While the magnification achieved is not high enough to clearly distinguish the morphology of the particles, the presence of rough edges indicates the possibility of truncated rhombic dodecahedron (or rhombic dodecahedron) shapes, as predicted by the literature (Zhang et al., 2018).

To gauge the effect of temperature on the structure of the ZIF-8, the previous synthesis (htZIF-8) was carried out at room temperature. All other synthetic variables (Zn:Hmim ratio, solution volume and composition, stirring and washing) remained constant. The following Figure illustrates the material obtained (named rtZIF-8 3):

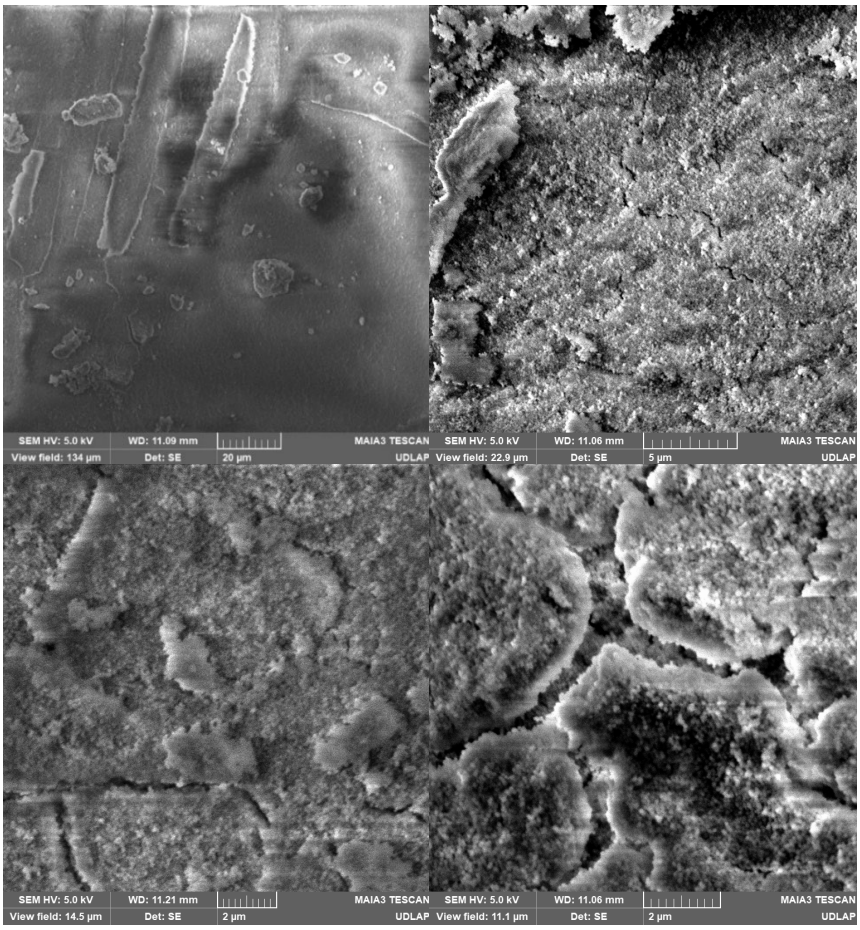

Figure 11. SEM micrographs for the rtZIF-8 3 material

For room temperature nucleation the ZIF-8 crystals retain an approximate diameter of 100 nm with acceptable homogeneity. Notice that in parallel with the other room temperature materials, the crystals are aggregated into bundles of densely packed ZIF-8, in contrast with the well-defined rhombic dodecahedrons of the htZIF-8.

A partial explanation of the greatly varying morphologies and sizes obtained for each ZIF-8 can be given by the nucleation mechanism involved at those specific synthetic parameters. In the case of the rtZIF-8 1 synthesis, Allegretto et al., 2024 establishes that the nucleation and growth of ZIF-8 follows classical nucleation theory: at such low ligand concentrations the diffusion and interaction of species in the reaction mixture becomes the defining step. Furthermore, for low supersaturation regimes (as is the case for the rtZIF-8 1 synthesis), individual ZIF-8 precursors bind onto energetically favorable points in a so-called *mononuclear regime*. By that, the particles form well established edges, favoring highly faceted geometries and larger diameters (in accordance with the micrographs depicted in Figure 5). Nevertheless, the stoichiometric 1:2 Zn:Hmim ratio simply does not provide enough ligand contact with metallic centers to promote the generalized growth of ZIF-8, possibly explaining the low yield obtained.

On the other hand, for higher molar ratios more complex growth mechanisms are said to occur. The saturation regime causes the formation of amorphous aggregates or clusters, which then suffer internal reorganization processes that yield small diameter nanoparticles. The abundance of species in close proximity to each other promotes *polynuclear growth*, favoring rapid, kinetic driven formation of ZIF-8 crystals (Allegretto et al., 2024).

The argument for a polynuclear growth regime might be backed by comparing the crystalline size of the ZIF-8 particles with their crystallite size. The calculation of the crystallite using the Scherrer equation was carried out in accordance with the literature using the Scherrer equation (Akhundzadeh et al., 2021; Ghorbani et al., 2020):

$$D = \frac{k \cdot \lambda}{B \cdot cos\theta}$$

Where $k$ is the crystallite-shape factor with magnitude values 0.8 and 1 (0.94 in this case), λ is the incident X-Ray wavelength, for copper λ = 0.15406 nm, $B$ is the full width at half maximum (FWHM) in radians and $\theta$ is the Bragg angle. The FWHM values were recovered using a Gaussian peak fitting of the (011) band, as can be seen in the following Figure:

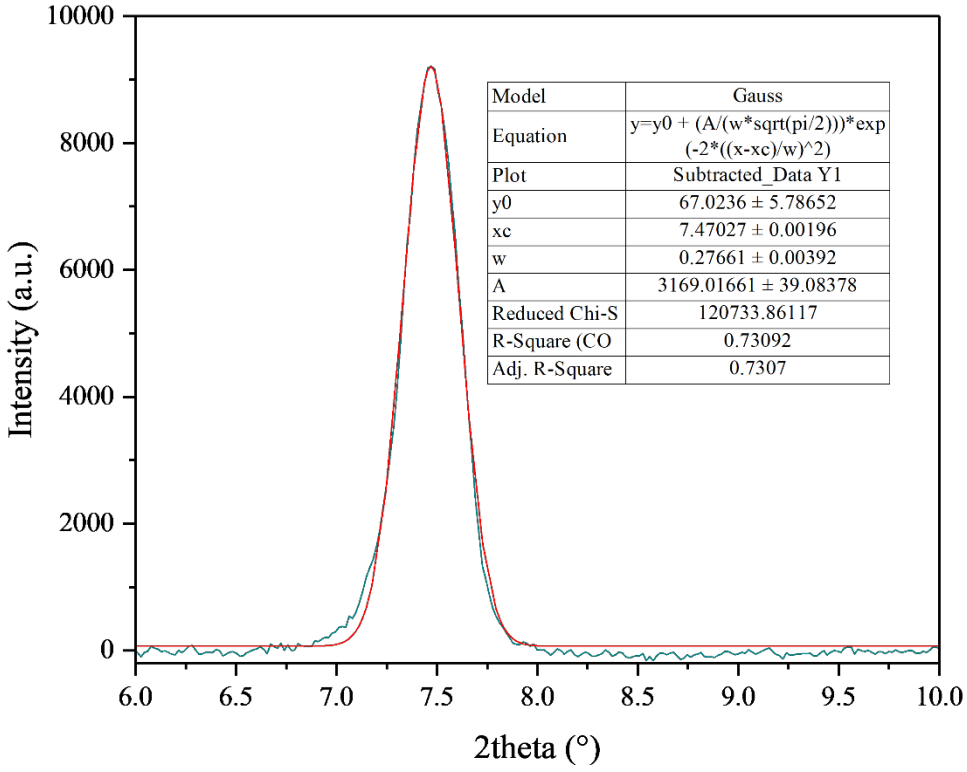


Figure 12. Gaussian fitting of the (011) peak for one the htZIF-8 samples.

Table 4. Information recovered from the Gaussian fitting. Computed using OriginLab Software.

| | | Value | Standard Error | t-Value |
|---|---|---|---|---|
| **htZIF-8** | y0 | 67.0236 | 5.78652 | 11.58272 |
| | xc | 7.47027 | 0.00196 | 3815.4455 |
| | w | 0.27661 | 0.00392 | 70.49878 |
| | A | 3169.01661 | 39.08378 | 81.08265 |
| | sigma | 0.13831 | 0.00196 | |
| | FWHM | 0.32568 | 0.00462 | |
| | Height | 9141.02911 | 112.14159 | |

From Figure , $\theta$ can be determined as half the *xc* value (since the x-axis itself is 2θ):

$$\theta = \frac{xc}{2} = \frac{7.470}{2} = 3.735°$$

Again, from Figure  the value of the FWHM (w) is recovered as 0.32568.

$$B = \frac{\text{FWHM} \cdot \pi}{180} = \frac{0.32568 \cdot \pi}{180} = 0.0082\ rad$$

Substituting in the Scherrer equation:

$$D = \frac{k \cdot \lambda}{B \cdot cos\theta} = \frac{0.94 \cdot 0.15406\ \text{nm}}{0.0057\ rad \cdot \cos(13.32253°)} = \ 25.46\ nm$$

Repeating the process for different htZIF-8 samples (pictured in Figure 9), crystallite sizes of 21.032 and 37.21 nm were calculated. These values confirm that the ZIF-8 particles observed in Figure 10 (with an estimated average diameter of around 100 nanometers) are actually polycrystalline, composed of 2-3 crystallite domains in average, corroborating a polynuclear growth regime.

When comparing the htZIF-8 and rtZIF-8 3 materials, it becomes clear that the influence of temperature is less involved in the morphology of the ZIF-8 crystals, affecting rather their "secondary" arrangement, i.e. formation of bundles. Therefore, higher temperatures, imparting higher kinetic energy into the system, result in defined ZIF-8 crystals constantly moving around and settling independently of each other. On the contrary, lower temperatures promote a sort of "lazy" or gradual settlement of crystals, which yield ZIF-8 clumps.

By considering the behavior herein observed, in conjunction with the mechanisms proposed in the literature, it can be broadly stated that: as the growth mechanisms shift from simplistic approaches (like that of CNT) into more complex mechanisms (by effect of temperature and species concentration), the ZIF-8 crystals reduce in size and subject to spherization processes, whereby large, faceted crystals turn to low diameter, truncated dodecahedron-like morphologies:

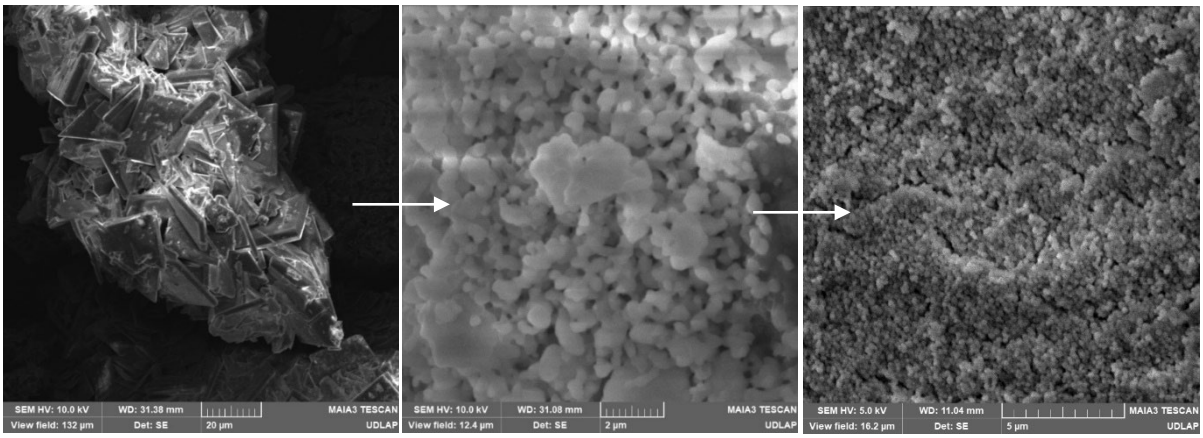


Figure 13. ZIF-8 crystal morphology and size evolution as a function of synthetic parameters. Left: rtZIF-8 1. Middle: rtZIF-8 2. Right: htZIF-8.

**htZIF-8 Raman Characterization**

The XRD spectrum for the high temperature ZIF-8 was recovered:

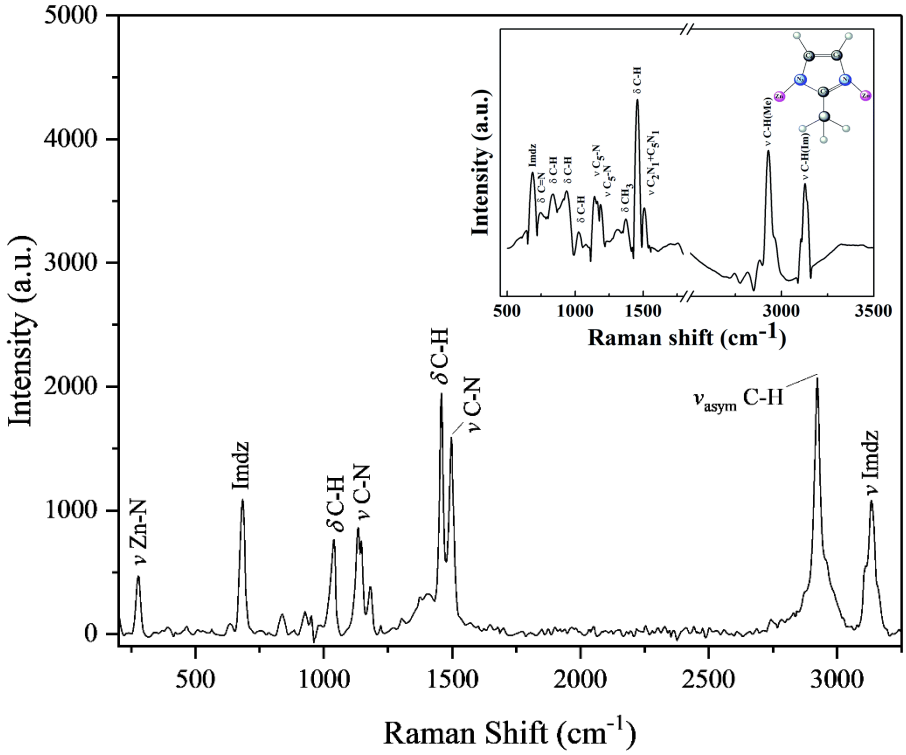


Figure 14. Raman spectrum for the synthesized ZIF-8 sample. Insert: ZIF-8 Raman spectrum (Li et al., 2020)

The Raman spectra of the synthesized ZIF-8 shows a good resemblance with that of the literature, as illustrated by the insert in Figure 14. A detailed comparison of band positions between samples is given:

Table 5. Raman active bands of ZIF-8 (Li et al., 2020; Kumari et al., 2013)

| **Raman Shift ($cm^{-1}$):** | | **Nature:** |
|---|---|---|
| **Literature** | **Own** | |
| 273 | 279 | Zn-N stretching |
| 686 | 683 | Out-of-plane movement of imidazole ring |
| 1021 | 1038 | C-H out of plane bending |
| 1146 | 1134 | C-N stretching |
| 1458 | 1458 | Methyl bending |

| | | |
|---|---|---|
| 1499 | 1496 | C-N stretching |
| 2930 | 2922 | Asymmetric methyl stretching |
| 3131 | 3134 | Imidazole ring stretching |

The band population is mainly defined by the peaks related to the organic ligand structures, most notably the imidazole ring bands at 683, 1134, 1496 and 3134 $cm^{-1}$.The Zn metal center is accounted for by the Zn-N band at 279 $cm^{-1}$. Minor deviations in the Raman shift in comparison with the literature, coupled with accurate peak intensity and shape, help corroborate that the synthesized material is of good quality.

**htZIF-8 FTIR Characterization**

Likewise, the composition of the synthesized ZIF-8 was corroborated via Fourier Transform Infrared spectroscopy (FTIR). The spectrogram recovered is shown:

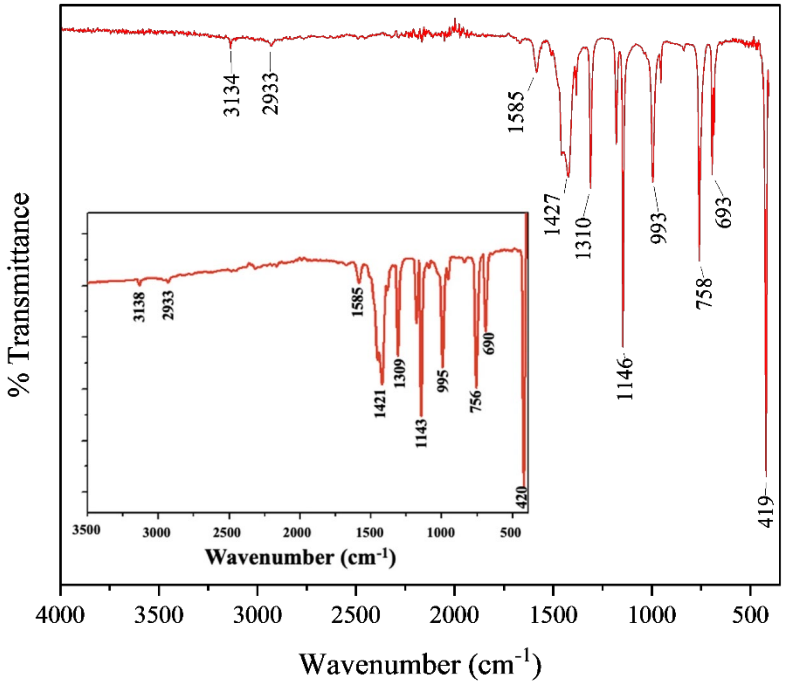


Figure 15. FTIR spectrogram for the synthesized ZIF-8 material. Insert: FTIR spectrogram for ZIF-8 (Mittal et al., 2022).

The FTIR spectrum is characterized (much like Raman), by the IR active modes of the Hmim ligands, particularly whole Imidazole ring movements and the characteristic carbon-nitrogen bond stretching. The inclusion of zinc is signalized by the band at 419 $cm^{-1}$, distinctive of the Zn-N bond found in the ZIF-8 primitive cell. Table 6 summarizes the bands found in the literature in contrast with the experimentally determined.

Table 6. IR active bands of ZIF-8 (Mittal et al., 2022)

| **Wavenumber ($cm^{-1}$):** | | **Nature:** |
|---|---|---|
| **Literature** | **Own** | |
| 420 | 419 | Zn-N stretching |
| 690 | 693 | Out-of-plane Imidazole ring bending |
| 756 | 758 | |
| 995 | 993 | |
| 1143 | 1146 | In-plane Imidazole ring bending |
| 1309 | 1310 | |
| 1421 | 1427 | Imidazole ring stretching |
| 1585 | 1585 | C=N stretching |
| 2933 | 2933 | Imidazole *al* C-H stretching |
| 3138 | 3134 | Imidazole *ar* C-H stretching |

*ar = aromatic, al = aliphatic

Due to the rigorous characterization processes undertaken, it can be safely stated that the synthesized ZIF-8 samples, particular that of the htZIF-8 route, displays the typical attributes related to a high-quality material, namely high crystallinity, adequate yield, and the presence of defining IR and Raman groups. Exceptional replicability opens the pathway into composite material development.

**htZIF-8 Surface Area**

A BELSORP-Mini II instrument was used to determine the *BET* (Brunauer-Emmett-Teller) surface area of the high temperature ZIF-8. The following Figure shows the recovered BET isotherm for the htZIF-8 sample (20.5 mg were used, with a saturated vapor pressure of 81.3 kPa):

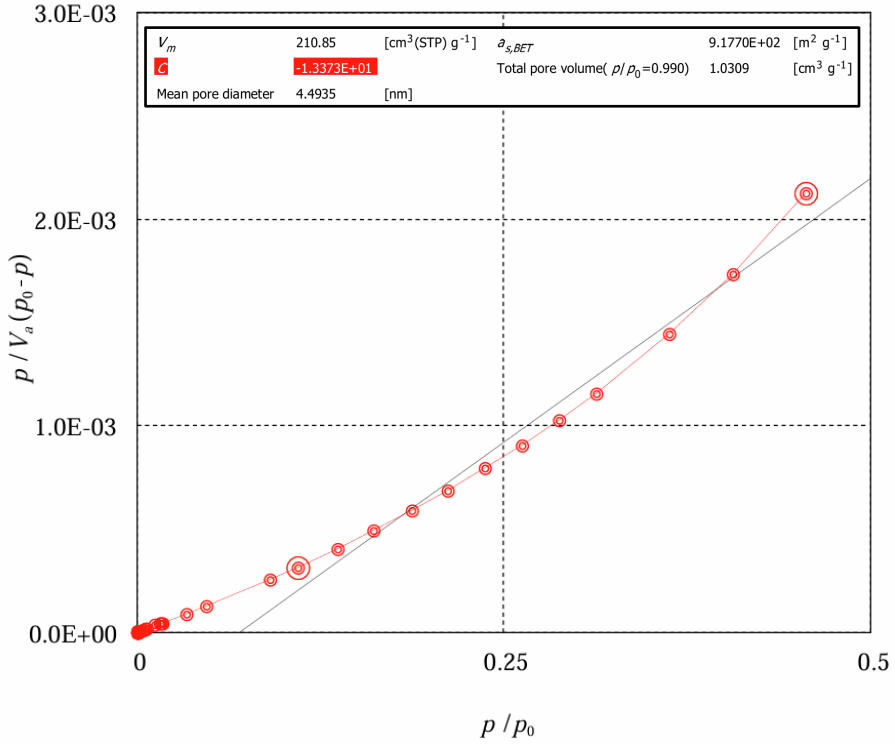


Figure 16. BET adsorption isotherm for the htZIF-8. Recovered from the BELSORP data analysis software.

The previous graph obeys the following linear equation, with the *P/Po* quotient corresponding to the *x* axis and *P/V(Po-P)* the *y* axis:

$$\frac{P}{V(P_o - P)} = \frac{1}{V_m C} + \frac{C-1}{V_m C} * \frac{P}{P_o}$$

Where *Vm* is the maximum adsorption volume, *V* is the volume of nitrogen at a given relative pressure (*P/Po*) and *C* is a constant. Following the linear equation form, it is deduced that the slope *m* and *y* intercept are equal to:

$$b = \frac{1}{V_m C};\ V_m = \frac{1}{b * C}$$

$$m = \frac{C - 1}{V_m C}; C = \frac{m}{b} + 1$$

From that, the surface area is calculated using:

$$S = Am * \frac{Vm}{22.4\ L} * N_A$$

Where the surface area *S* depends on Avogadro's number $N_A$, the volume at standard conditions (22.4 L) and the cross-sectional area of an adsorbate molecule, *Am*. From Figure 16, the surface area of the material is calculated to be 917.7 $m^2/g$, with a pore diameter of 4.49 nm. These values evidence the great capacity of ZIF-8 to intake eugenol, highlighting its importance as a eugenol diffusion agent within the final composite.

## NcZ Composites

### NcZ XRD and SEM Characterization

The loading of ZIF-8 onto the carboxymethyl cellulose fibers was primarily determined by XRD and SEM characterization of the resulting composite. In the case of XRD, the composite's diffractogram was expected to appear as a superposition of both species' spectra, signalizing an adequate inclusion of ZIF-8 and cellulose fibers. The spectra for NcZ composites featuring rtZIF-8 and htZIF-8 are shown below:

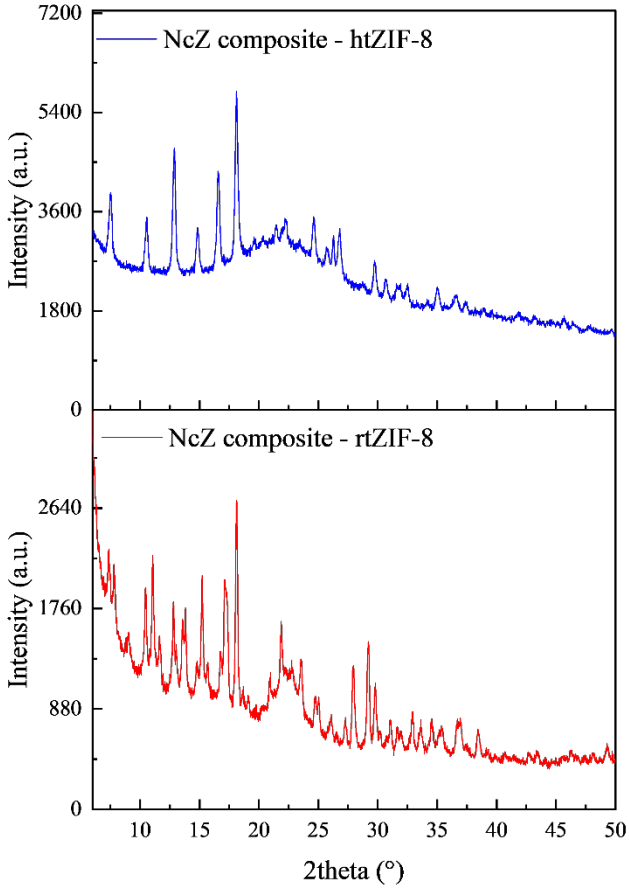


Figure 17. XRD spectra for the generated composites.

Furthermore, a direct comparison between the composites and the source ZIF-8 appears in Figure 18. Notice that in each case, the NcZ samples retain the XRD peaks (both

in intensity and position) of the primigenial ZIF-8. The inclusion of carboxymethyl cellulose into the system is pointed out by the broad band with its peak at around 22.5° (Du et al., 2023).

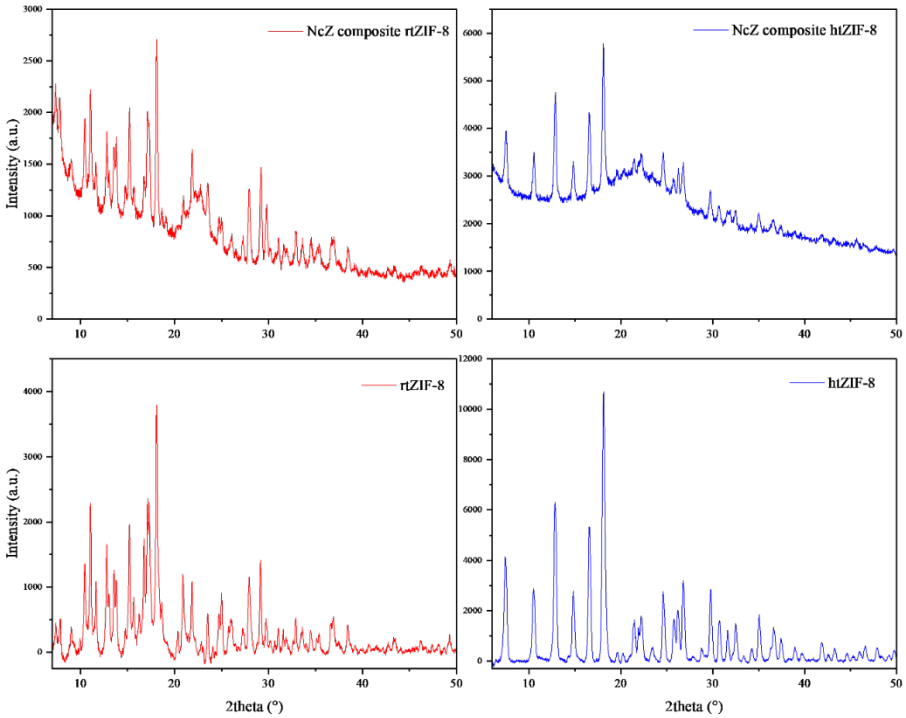


Figure 18. Comparison between the XRD spectra of the primigenial ZIF-8 (bottom row) and the resulting composite (top row).

Comparing said signal with a spectrum of carboxymethyl cellulose recovered from the literature:

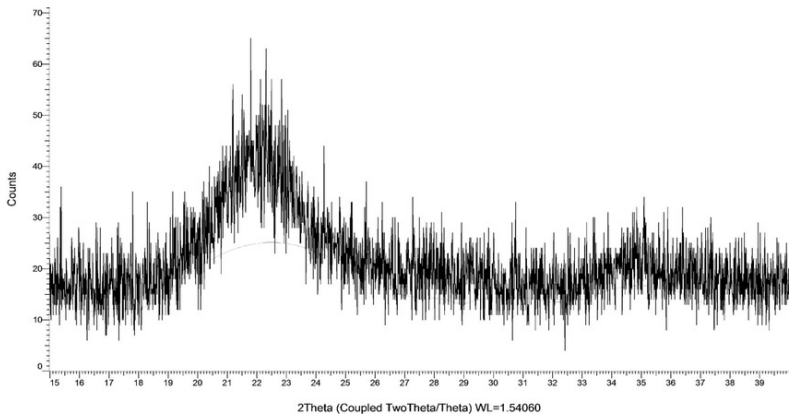


Figure 19. XRD spectrum for carboxymethyl cellulose (Abdulhameed et al., 2019)

From the previous XRD spectra it can be inferred that composite fabrication does not sacrifice the crystallinity of the MOF, while the inclusion *in situ* of the nanocellulose into the reaction mixture proved to be a time and resource effective synthetic route.

Moving onto SEM characterization of the NcZ1, NcZ2 and NcZ3 composites (recall that the ZIF-8 loading percentage by weight for each composite is 50, 25 and 12.5%, respectively). Starting with the NcZ1 material:

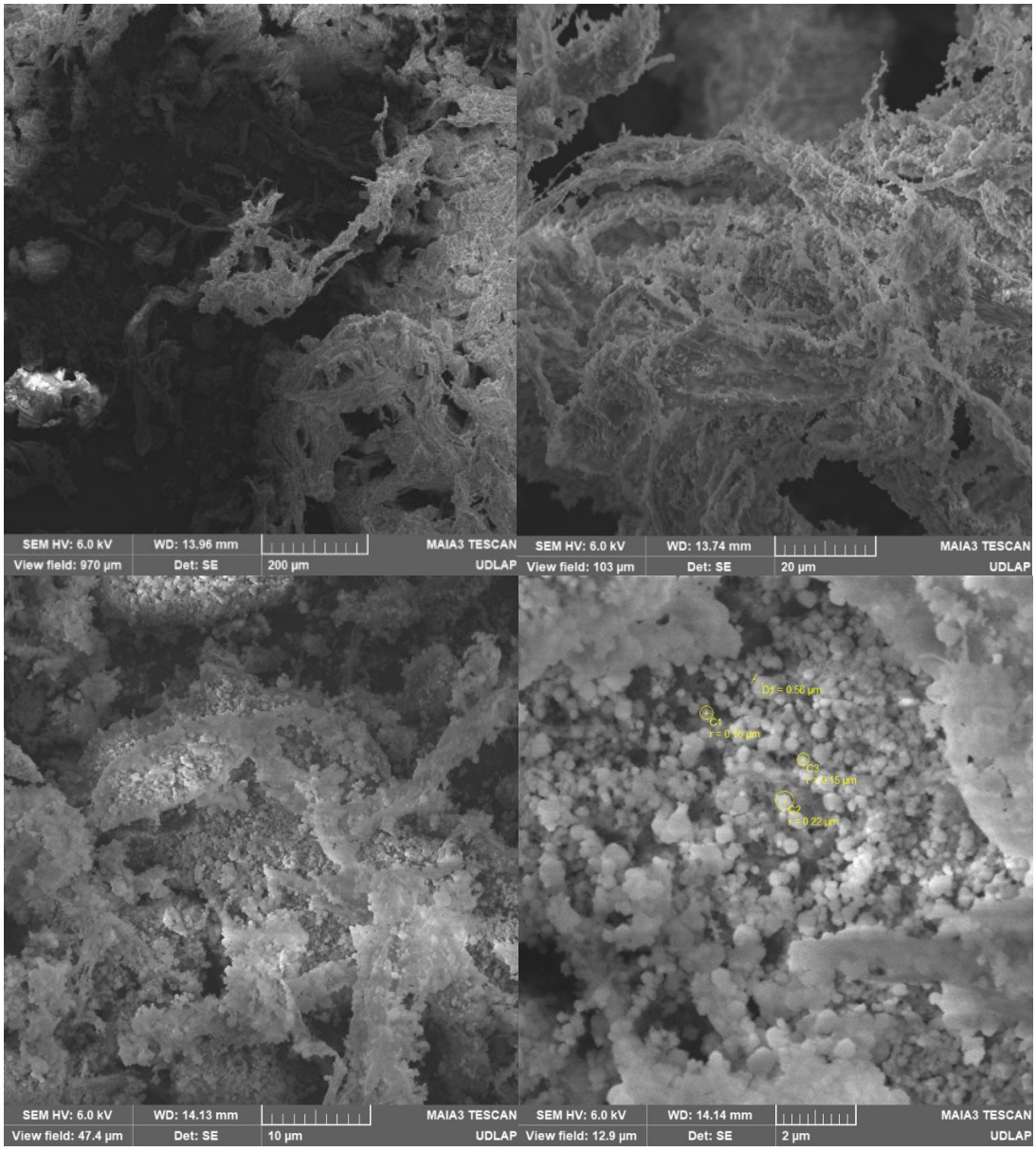

Figure 20. SEM micrographs recovered for the NcZ1 composite.

The following image corresponds to the NcZ2 composite:

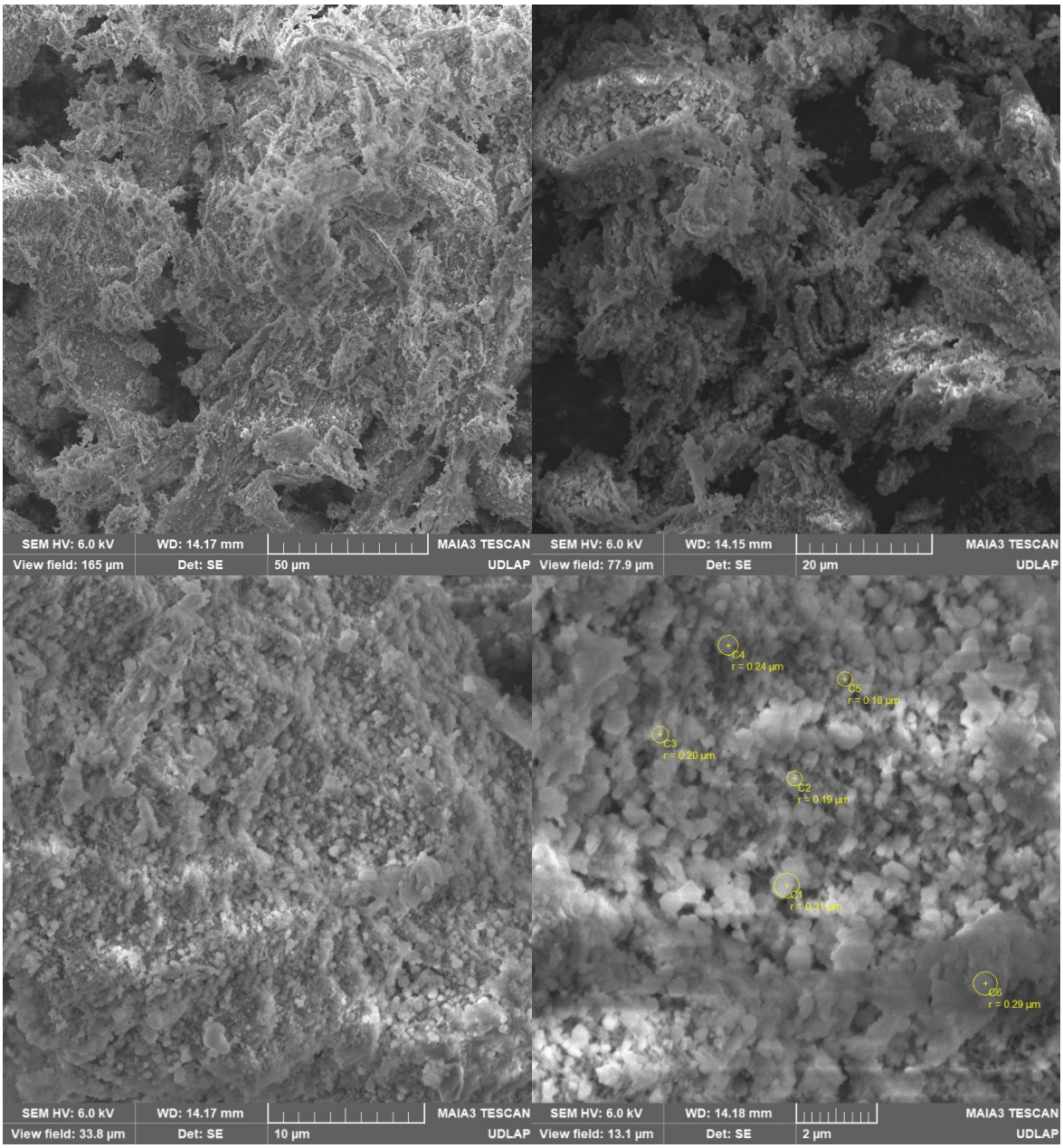


Figure 21. SEM micrographs recovered for the NcZ2 composite

And, finally, the micrograph depicting the NcZ3 composite:

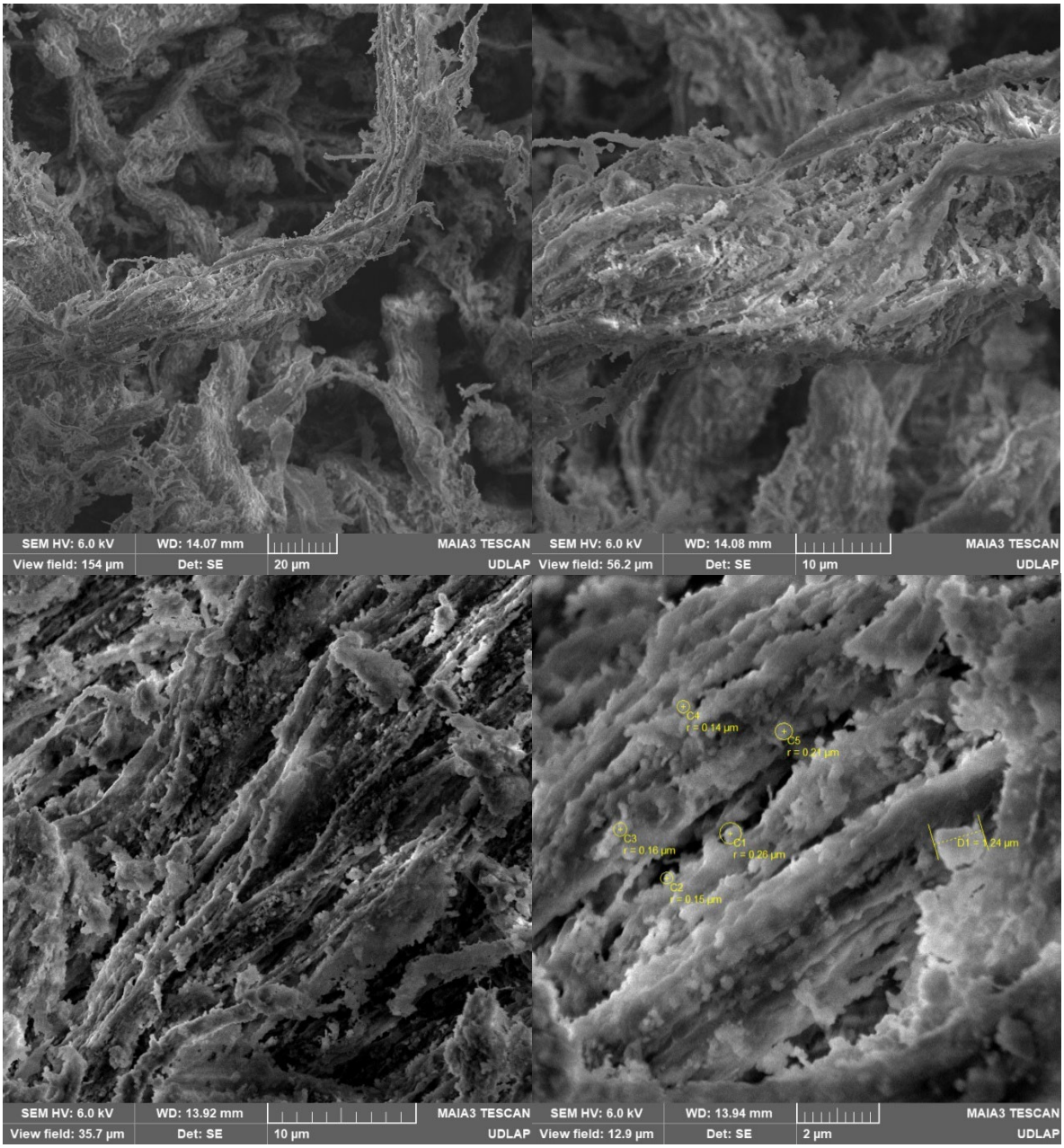


Figure 22. SEM micrographs recovered for the NcZ3 composite

There is a noticeable difference in the appearance of the composite as a function of the MOF loading percentage. Starting with the NcZ1 composite (50 % loading), a complete saturation of the fibrils with attached ZIF is observed. The case is similar for the NcZ2 composite, where an almost complete surface coverage is achieved by the ZIF-8. A

perceptible reduction of the ZIF-8 loading is not seen until a 12.5% weight loading (NcZ3 composite), where the surface of the fibrils can be clearly seen, and the ZIF-8 crystals are grown into the surface in a sporadic and distinct manner. From the previous Figures, the morphology and size distribution of the ZIF-8 crystals is said to be adequate: closely resembling the desired truncated rhombic dodecahedron but introducing some minor variations in shape and size.

Expanding on the aforementioned remark, two types of ZIF-8 crystals can be distinguished: those directly growing on the surface of the cellulose fibril, and those that nucleated off of previously grown crystals (or otherwise highly populated areas). For the first case, Figure 22 (NcZ3) shows fibrils occupied with isolated crystals of the highest perceived quality, with the visible population (qualitatively) showing acceptable likeness in both shape and size with the htZIF-8 material. Thus, at 12.5% loading the adsorbed Zn cations on the surface of the fibrils provide a suitable nucleation site, where growth occurs in a similar way to that of the htZIF-8.

On the other hand, Figures 20 and 21 (corresponding to the NcZ1 and NcZ2 samples) show a more heterodisperse population. Notice that the ZIF-8 crystals of familiar diameter occur in areas in contact with the substrate (nanocellulose), whilst larger particles lay on top of the crystals underneath. This “secondary” nucleated crystals, being loosely tethered to the particles below, endure imperfect growth, favoring slightly warped morphologies and oversized diameters.

## NcZ Energy Dispersive X-ray Spectroscopy

A quantitative insight into the elemental composition and spatial arrangement of the elements in the composite is given by Energy Dispersive X-ray Spectroscopy (EDX). The following figure shows the EDX spectrum recovered for a determined area of the NcZ1 composite:

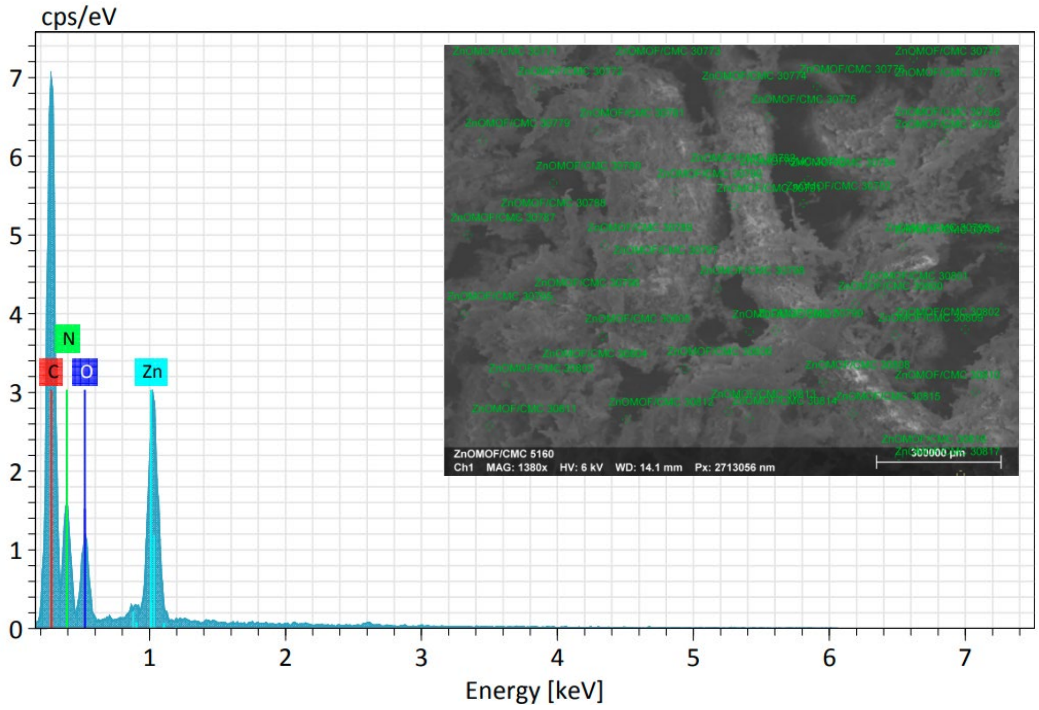


Figure 23. EDX spectrum for the NcZ1 composite. Insert: Microscope view of the surveyed area.

Table 7 summarizes the elemental composition of the selected area. Unsurprisingly, carbon comprises most of the normalized mass (45.32%), being the majority component of both the cellulose and the ligand (Hmim). Following in abundance are nitrogen and zinc in close proximity (22.7 and 21.1%, respectively). This quality is unexpected, as the ZIF-8 primitive cell is composed of a 1:3 ratio of Zn to N, with Zn weighing 1.55 times as much as N. This excess of nitrogen (which corresponds to a 1.09 weight surplus over Zn, and a 1:5 ratio of Zn to N) must come from an overpopulation of the ligand, Hmim. Such a fact might explain the physical characteristics of the ZIF-8 crystals in the NcZ1 and NcZ2 composites,

as an excess of unreacted ligand may induce the formation of larger particles with less defined morphologies.

Table 7. Elemental composition of the NcZ1 composite.

| Element | Mass % | Normalized Mass % | Atom % |
|---|---|---|---|
| Carbon | 77.49 | 45.32 | 58.99 |
| Nitrogen | 38.93 | 22.77 | 25.41 |
| Zinc | 36.14 | 21.14 | 5.055 |
| Oxygen | 18.44 | 10.78 | 10.54 |

Now, an EDX spectrum for the NcZ4 composite (6.25% weight loading) is shown:

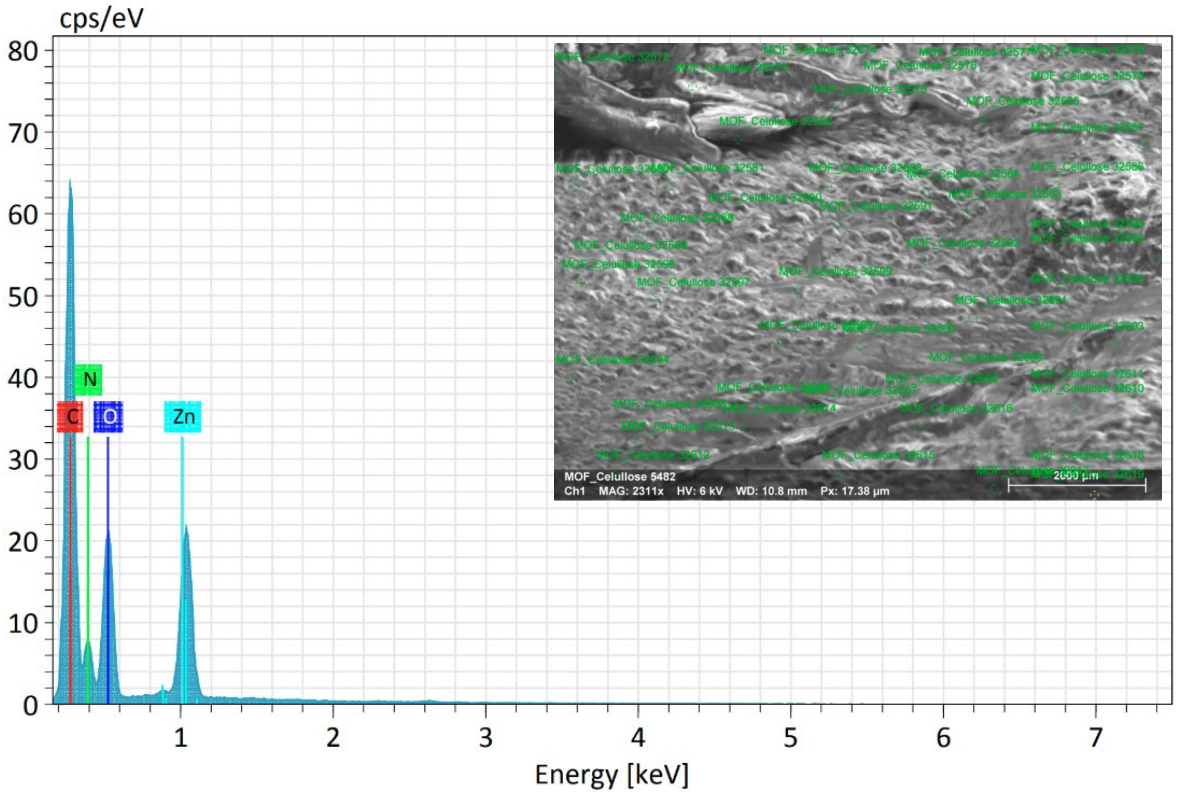


Figure 24. EDX spectrum for the NcZ4 composite. Insert: Microscope view of the surveyed area.

In comparison to the heavily loaded NcZ1 composite, the NcZ4 material exhibits an almost stoichiometric mass ratio of Zn to N (Table 8), at quotient of 1.31 in magnitude. This

quality proves that lower loading percentages promote the sole nucleation of more crystalline ZIF-8 particles, in accordance with the observations made with the SEM micrographs.

Table 8. Elemental composition of the NcZ4 composite.

| Element | Mass % | Normalized Mass % | Atom % |
|---|---|---|---|
| Carbon | 92.20 | 47.61 | 60.69 |
| Oxygen | 42.22 | 21.63 | 20.70 |
| Zinc | 34.10 | 17.47 | 4.09 |
| Nitrogen | 25.93 | 13.29 | 14.52 |

The following Figure shows an EDX elemental map of the NcZ3 composite, notice how the elements are evenly distributed across the sample, indicative of a good ZIF-8 formation:

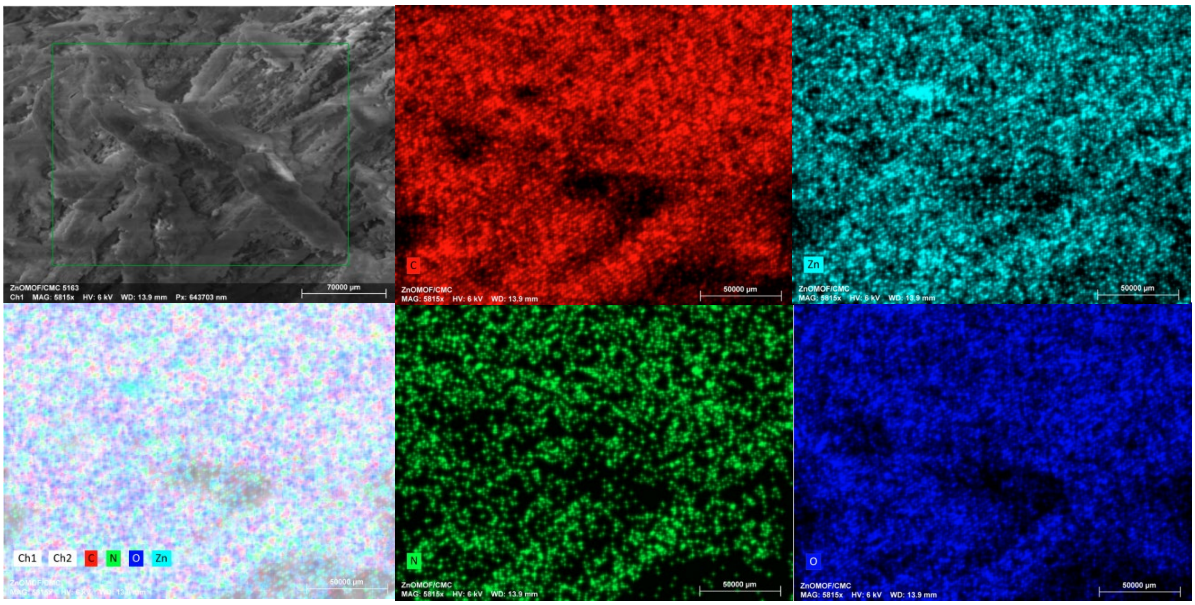


Figure 25. EDX elemental map of the NcZ3 composite

**Composite's physical properties as a function of their humidity level before lyophilization**

As stated in the methodology section, the composite's final physical properties were gauged as a function of their humidity level before the freeze-drying step. Namely, two variants of this process were conducted: humid composites and dry composites. Humid composites refer to materials in which some solvent was left inside the porosities of the sample, i.e. no effort was made to further dry the composite aside from removing the excess solvent from the washing step. Consequently, dry composites are those samples in which the majority of the solvent was removed by drying at room temperature for 48-72 hours prior to lyophilization.

This variation resulted in two different types of composites fabricated, the first type being cotton-like composites (like the ones micrographed in Figures 20-22) originating from humid precursors. "Cotton-like" refers both to its macroscopic and microscopic appearance, displaying a main body composed almost exclusively of cellulose fibrils intertwined into an agglomerate. This composite appears soft to the touch, presenting low mechanical strength, reminiscing of fibrous materials like cotton (naturally), oakum, hemp, etcetera. The following Figure shows the aforementioned structure:

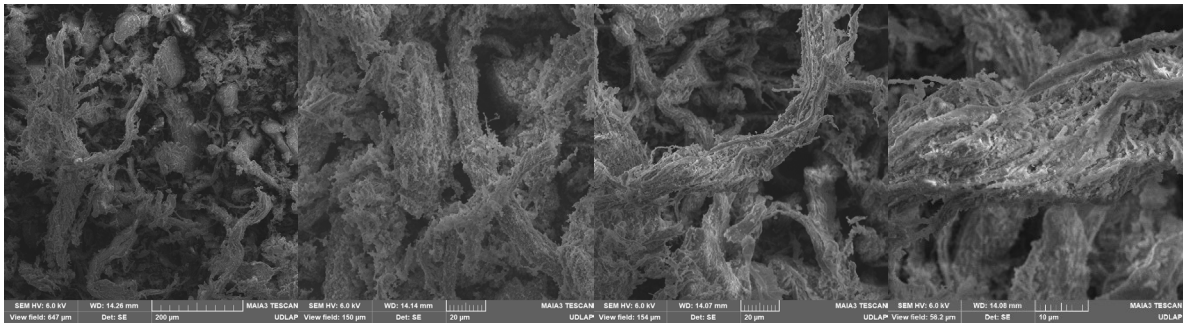

Figure 26. Fibrous structure of the humid composites.

On the contrary, the dry composite yielded a hard, rock-like material both in appearance and to the touch, appearing to be much denser than the cotton-like composite. Figure 27 shows the appearance of the rock-like composite under the microscope:

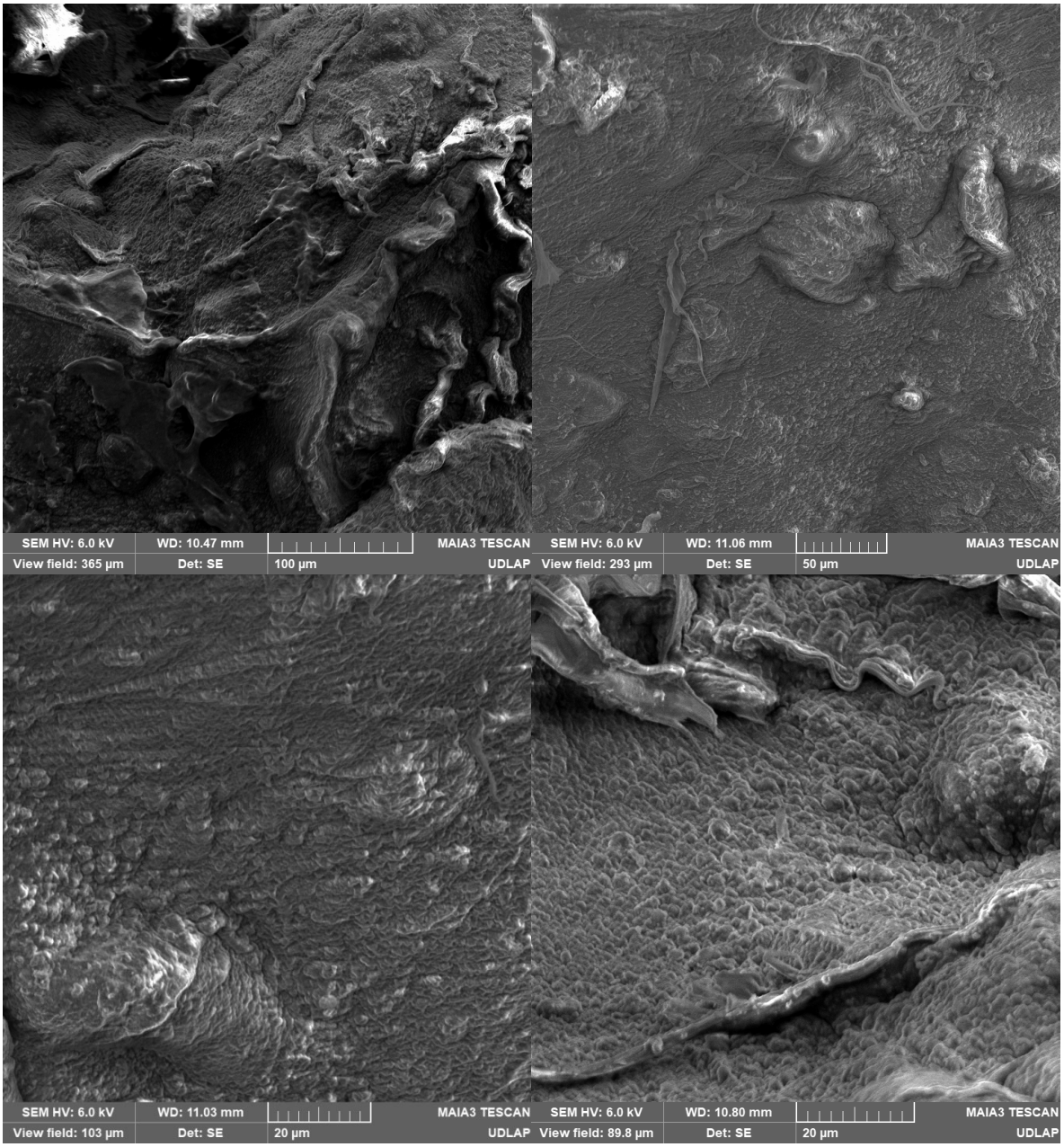


Figure 27. Microscopic structure of the dry composites.

Note that the cellulose appears to have bound together, forming a continuous structure spanning into the micrometer range. The fibrous structure seen before is no longer present, even though ripples, possibly coming from the tight compression of cellulose fibers, can be distinguished. This extreme variation in the microscopic arrangement of the material might explain the enhanced physical properties of the dry composite, acting under stress as a solid scaffolding rather than a fibrous material.

The resulting cross-linking of the nanocellulose fibrils might be the result of high temperatures and low pressures coupled with the total or near total absence of liquid in the matrix. Similar processes include the dehydrothermal treatment commonly used to enhance the stability and compression strength of collagen (Yang et al., 2023).

**Composite's swelling degree and water stability**

Swelling tests were performed on the dry composites introduced in the previous section. More specifically, NcZ1 and NcZ4 composites were used, corresponding to 50% and 6.25% ZIF-8 loading of the cellulose fibrils respectively. In brief, the composites were placed in an aqueous medium for 45 minutes at room temperature without stirring. Their weight was recorded before and after the water treatment for further calculations. The following figure shows the NcZ4 composite before and after the procedure:

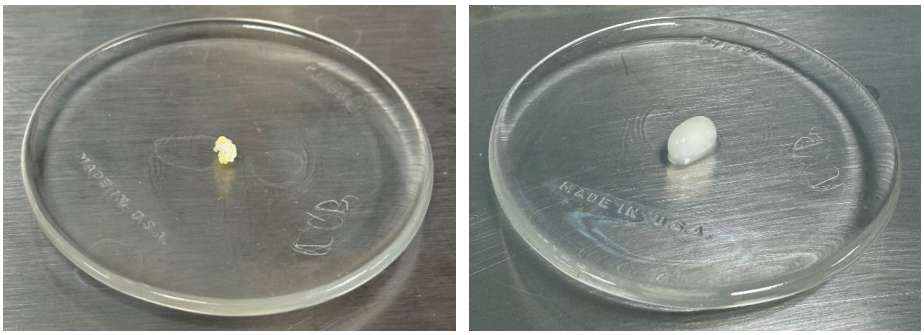

Figure 28. Appearance of the NcZ4 composite before (left) and after (right) the swelling test.

After 45 minutes submerged in water, the composite demonstrates clear swelling, evidenced by the augmented volume and the transition from a rocky, jagged appearance to a more streamlined pill-like shape. The structural robustness of the material is highlighted by a lack of delamination or excessive deformation of the composite. Figure 29 further expands this idea by showing that even after 45 minutes under water, there is no noticeable diffusion of composite material into the surrounding aqueous environment. The transparent character of the water indicates that no ZIF-8 detached from the fibrils and permeated to the water, corroborating the strongness of the ZIF-8/cellulose bond at lower loading percentages and the overall stability of the composite material in water.

Figure 29. Aqueous test environment before (left) and after (right) the swelling test.

In order to characterize the swelling response of the composite, its density was calculated using a modified hydrodensitometry method (McArdle et al., 2010), while its pore volume was computed via a liquid saturation method (Kazem, 2021):

$$\rho = \frac{M_A}{\frac{M_A - M_W}{D_W}}$$

And:

$$Pore\ volume = \frac{M_W - M_A}{D_W}$$

Where $M_A$ is the mass of the composite previous to being submerged in water, $M_w$ is the mass of the composite after the treatment and $D_W$ is the density of water. For this case, the density of water at the time of performing the test was taken at 0.997 g/ml (corresponding to a temperature of 22°C). Substituting:

$$\rho = \frac{M_A}{\frac{M_W - M_A}{D_W}} = \frac{0.021\ g}{\frac{0.255\ g - 0.021\ g}{0.997\ \frac{g}{ml}}} = 0.089\ \frac{g}{ml}$$

$$Pore\ volume = \frac{M_W - M_A}{D_W} = \frac{.255\ g - 0.021\ g}{0.997\ \frac{g}{ml}} = 0.234\ ml$$

From the previous equations various aspects are of interest: firstly, the composite's mass increases by 234 mg, evidencing the great absorption capacity of the fabricated material. The swelling seen in Figure 28 corresponds to a volume augmentation of 0.234 ml, which yields a decrease in density to about 0.089 g/ml. This indicates that the rehydration of the dry composites effectively opens up the cellulose matrix, which in turn has a great liquid intake capacity without sacrificing the structural integrity of the cellulose matrix or the loaded ZIF-8.

Now, for the NcZ1 composite the material's larger ZIF-8 loading became apparent, as the ZIF-8 clearly diffused into the water, as observed in the following Figure. Note that as time advances the water becomes much cloudier, evidencing the gradual release of MOF into the environment.

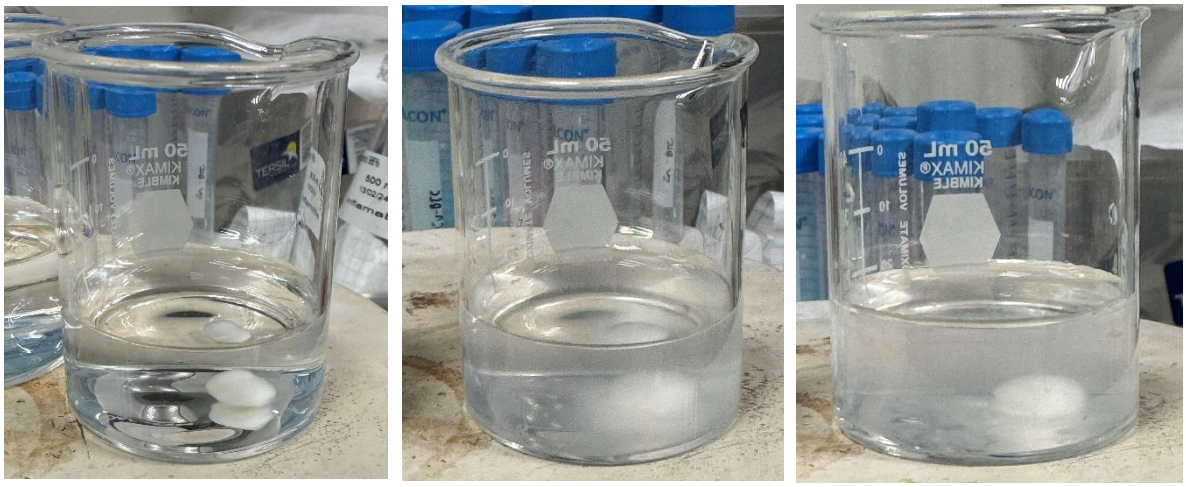

Figure 20. ZIF-8 permeation into the water. Left: 10 minutes into the test. Middle: 30 minutes into the test. Right: 45 minutes into the test

This deterioration in water stability might arise from the observation made before: for higher MOF loadings, an important amount of ZIF-8 is growth atop of previously nucleated ZIF-8 crystals. Ultimately, these ZIF-8 crystals detached from the nanocellulose fibrils have

a far worse adhesion to their surroundings, being more easily diffused into the aqueous environment. Nonetheless, as seen in the following image, the composite retains its shape after being retrieved from the water, signalizing that the structural properties of the composite are not changed for a higher MOF loading.

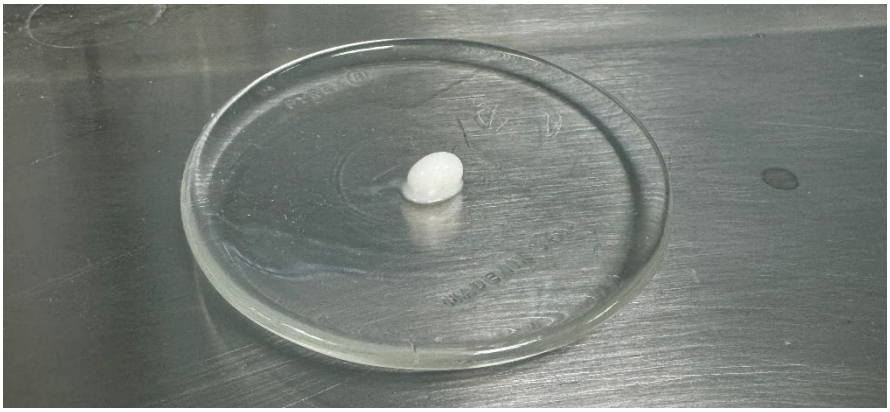

Figure 31. NcZ1 composite after the swelling test.

**Antimicrobial activity**

The well-diffusion antibacterial assays were performed by Rosa Hernández of the Department of Chemical, Food and Environmental Engineering, UDLAP. The evaluation was carried out using S. aureus due to its prevalence: being the most common cause of nosocomial bacteremia in North and Latin America and the second most common in Europe (Pasachova et al., 2019). The following image shows the inhibition halos recovered for the NcZ1 composite:

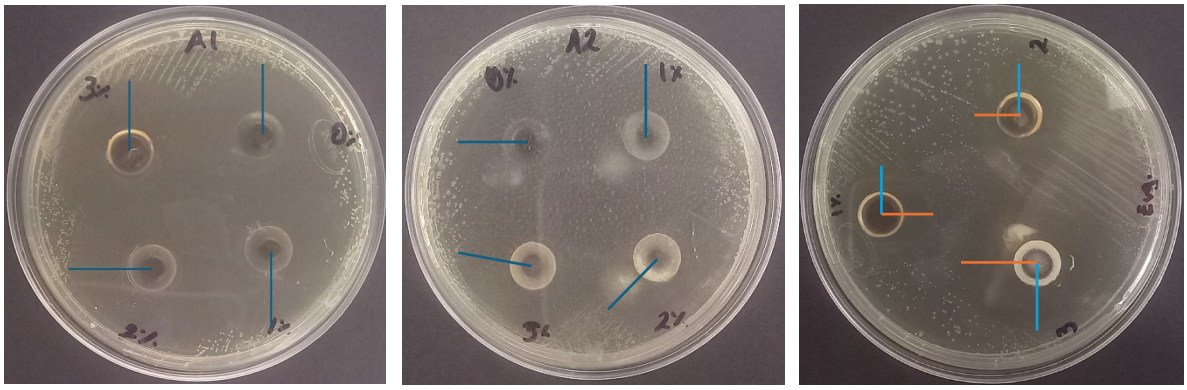


Figure 32 Left and middle: Inhibition assays performed for two different NcZ1 composites. Right: eugenol control.

Starting with the left-hand side image, four distinct inhibitions can be seen for each zone: 3% eugenol impregnation (top left zone), 2% (bottom left), 1% (bottom right) and 0% eugenol, which corresponds to virgin composite (top right). Notice that the virgin composite shows significant performance in comparison with its eugenol-functionalized counterparts. This antimicrobial activity might be due to the ZnO moieties absorbed on the surface of the cellulose fibrils (Sirelkhatim et al., 2015). Similar behavior is also present in the NcZ1-2 assay, demonstrating the material's robustness. On the other hand, the eugenol controls (3, 2 and 1 %) depicted in the leftmost image yield smaller inhibition zones, demonstrating the positive effect of the composite as a substrate in comparison to the virgin active compound.

Figure 33 represents the antimicrobial activity of the NcZ2 composites along four separate assays. A priori, the inhibition halos are smaller in comparison to the NcZ1 composite for the same eugenol loading as before. This might evidence that less ZIF-8 in the material limits the amount of eugenol available to diffuse in the growth medium.

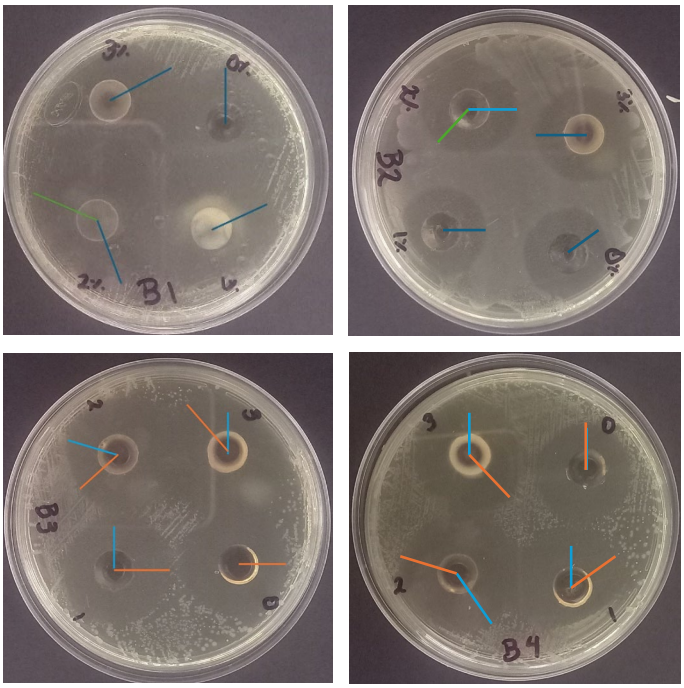


Figure 33. Inhibition assays performed for four different NcZ2 composite samples.

The antimicrobial character of the composite is seen across all assays, signified by the clear presence of an inhibition halo in the growth medium. Remarkable reproducibility is achieved in all trials, with constant sized inhibition zones across the majority of the samples, with the exception of the top-right assay.

Finally, the following figure shows the antimicrobial activity of the NcZ3 composite. Notice that there is not a noticeable reduction of the inhibition halo with respect to the last material, nonetheless, more assays are required to verify this property.

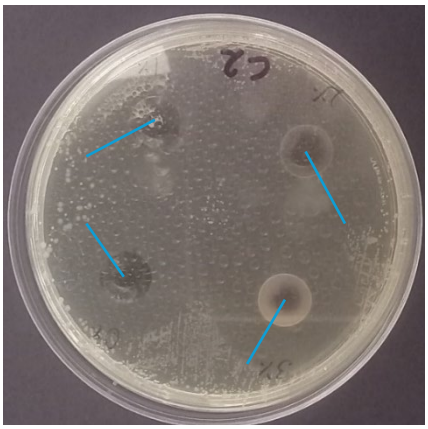

Figure 34. Inhibition assay performed for the NcZ3 composite

Notice that for all cases (NcZ1-3 composites) the diameter of the inhibition halo appears to be independent of the eugenol loading (or marginally affected by it) that is; with the inhibition zones for 3% loading presenting similar sizes to those of 2% and 1% eugenol content. This might indicate a) a limit to the amount of eugenol effectively incorporated into the composite or b) a limit to the amount of eugenol that can effectively diffuse into the medium. Nonetheless, this peculiarity presents the opportunity to maintain the performance of the system while reducing the amount of essential oil by a third.

All composites, invariable of their ZIF loading, exhibited larger inhibition halos in comparison with the control eugenol assay. This demonstrates the capability of the NcZ composites to absorb an important quantity of eugenol and facilitate its diffusion in the medium, resulting in better antimicrobial efficacy.

## Conclusions

The aqueous methodology at room pressure herein adopted presents itself as an excellent way to synthesize ZIF-8, overcoming much of the challenges of traditional solvothermal and microwave synthetic routes (i.e. resource and time efficiency), without sacrificing crystallinity and yield. In addition to the above, the lack of specific equipment, harmful solvents and high yield make the aforementioned methodology environmentally friendly and on par with the principles established by green chemistry (American Chemical Society, n.d.). Added to the above, a diverse set of ZIF-8 embedded nanocellulose composites (NcZ composites) were generated, exhibiting a rich variety of MOF loadings and physical attributes. This tunability of the final composite's characteristics poses an interesting prospect, giving the ability to tailor-make materials in order to meet specific needs.

Finally, the NcZ composites displayed good antimicrobial activity, forming distinct inhibition halos across multiple *S. aureus* growth mediums in a well-diffusion assay. The diameter of said inhibition zones changed as a function of the ZIF-8 loading percentage and not the eugenol concentration. The NcZ3 composite, with 50% weight loading, consistently yielded the biggest inhibition areas as more eugenol could be stocked into the composite for later diffusion.

These results further corroborate the potential of ZIF/Cellulose-based composites for food sector applications: providing substantial antimicrobial activity while being otherwise innocuous, easy to synthesize and resource effective.

**Recommendations**

Further understanding of the NcZ composites is required, mainly the material's thermal stability and adsorption capacity, the latter achieved by Brunauer-Emmett-Teller (BET) adsorption. While partial understanding of the nature of the ZIF-8 loading into the cellulose was achieved by EDX, a precise Thermogravimetric analysis (TGA) would give extra insight into the effectiveness of the ZIF-8/cellulose interaction, enabling the possibility to determine the loading yield of ZIF-8 into the matrix.

Regarding the antimicrobial activity of the composite, more assays are needed to properly characterize the inhibition properties of each composite as function of their loading percentage, especially regarding the NcZ3 composite.

**References**

Hunger. (n.d.). Food and Agriculture Organization of the United Nations.http://www.fao.org/hunger/en/

World Food Programme. (n.d.). Hunger Map Live. https://hungermap.wfp.org/

Causes of hunger. (n.d.). Action Against Hunger. https://www.actionagainsthunger.org/the-hungercrisis/the-causes-of-hunger/

Consejo Nacional de Evaluación de la Política de Desarrollo Social (CONEVAL). (s.f.). Medición de pobreza 2022. Retrieved July 26, 2024, from https://www.coneval.org.mx/Medicion/MP/Paginas/Pobre za 2022.aspx

Consejo Nacional de Evaluación de la Política de Desarrollo Social (CONEVAL). (s.f.). Pobreza a nivel municipio 2010-2020. Retrieved July 26, 2024, from https://t.ly/2Y7s-

Soto J. (16 de octubre, 2020). ¿Cuánta comida se desperdicia en el mundo y como afecta al planeta? Greenpeace. https://www.greenpeace.org/mexico/blog/9103/cuantacomida-se- desperdicia-en-el-mundo-y-como-afecta-alplaneta/

[7] Food and Agriculture Organization of the United Nations. (s.f.). Basic Knowledge for Food Technology. https://www.fao.org/4/AD379E/AD379E02.htm

Fung, D. Y. C. (2009). Food spoilage, preservation and quality control. In Encyclopedia of Microbiology (pp. 54–79). Elsevier. https://doi.org/10.1016/B978- 012373944-5.00122-X

Fung D. Y. C., Kastner CL, Lee CY, Hunt ML, Dikeman ME, and Kropf D (1980) Mesophilic and psychotropic populations on hot boned and conventionally processed beef. Journal of Food Protection 43: 547–550.

Rezaei M., Liu B. (2017). Food Loss and Waste in the Supply Chain. FAO. https://openknowledge.fao.org/server/api/core/bitstream s/36cb45bc-392c-41fb-97f1-90ca1f16ee7f/content

K. Sonawane, S., P. Patil, S., S. Arya, S. (2018). Nanotechnology enrolment in food and food safety. Journal of Microbiology, Biotechnology and Food Sciences, 8(3), 893–900. https://doi.org/10.15414/jmbfs.2018-19.8.3.893- 900

Anees Ahmad, S., Sachi Das, S., Khatoon, A., Tahir Ansari, M., Afzal, Mohd., Saquib Hasnain, M., Kumar Nayak, A. (2020). Bactericidal activity of silver nanoparticles: A mechanistic review. Materials Science for Energy Technologies, 3, 756–769. https://doi.org/10.1016/j.mset.2020.09.002

Bruna, T., Maldonado-Bravo, F., Jara, P., Caro, N. (2021). Silver nanoparticles and their antibacterial applications. International Journal of Molecular Sciences, 22(13), 7202. https://doi.org/10.3390/ijms22137202

Gudkov, S. V., Burmistrov, D. E., Serov, D. A., Rebezov, M. B., Semenova, A. A., Lisitsyn, A. B. (2021). A mini review of antibacterial properties of zno nanoparticles. Frontiers in Physics, 9. https://doi.org/10.3389/fphy.2021.641481

Mendes, C. R., Dilarri, G., Forsan, C. F., Sapata, V. de M. R., Lopes, P. R. M., de Moraes, P. B., Montagnolli, R. N., Ferreira, H., Bidoia, E. D. (2022). Antibacterial action and target mechanisms of zinc oxide nanoparticles against bacterial pathogens. Scientific Reports, 12(1), 2658. https://doi.org/10.1038/s41598-022-06657-y

Wexler, P. (Ed.). (2014). Encyclopedia of toxicology (Third edition.). Academic Press.

Jeyakumar, G. E., Lawrence, R. (2021). Mechanisms of bactericidal action of Eugenol against Escherichia coli. Journal of Herbal Medicine, 26, 100406. https://doi.org/10.1016/j.hermed.2020.100406

Noga, M., Milan, J., Frydrych, A., Jurowski, K. (2023). Toxicological aspects, safety assessment, and green toxicology of silver nanoparticles (Agnps)—critical review: State of the art. International Journal of Molecular Sciences, 24(6), 5133. https://doi.org/10.3390/ijms24065133

Di Martino, P. (2022). Antimicrobial agents and microbial ecology. AIMS Microbiology, 8(1), 1–4. https://doi.org/10.3934/microbiol.2022001

Hunger numbers stubbornly high for three consecutive years as global crises deepen: UN report. (2024). Retrieved August 31, 2024, from https://www.who.int/news/item/24-07-2024-hungernumbers-stubbornly-high-for-three-consecutive-years-asglobal-crises-deepen–un-report

Raptopoulou, C. P. (2021). Metal-Organic Frameworks: Synthetic Methods and Potential Applications. Materials, 14(2), 310. https://doi.org/10.3390/ma14020310

Claudio-Rizo, J. A., Cano Salazar, L. F., FloresGuia, T. E., Cabrera-Munguia, D. A., Claudio-Rizo, J. A., Cano Salazar, L. F., Flores-Guia, T. E., Cabrera-Munguia, D. A. (2021). Estructuras metal orgánicas (MOFs) nanoestructuradas para la liberación controlada de fármacos. Mundo nano. Revista interdisciplinaria en nanociencias y nanotecnología, 14(26). https://doi.org/10.22201/ceiich.24485691e.2021.26.69634

Cellulose. (n.d.). American Chemical Society. Retrieved August 26, 2024, from https://www.acs.org/molecule-ofthe-week/archive/c/cellulose.html

Manoukian, O. S., Sardashti, N., Stedman, T., Gailiunas, K., Ojha, A., Penalosa, A., Mancuso, C., Hobert, M., Kumbar, S. G. (2019). Biomaterials for tissue engineering and regenerative medicine. In R. Narayan (Ed.), Encyclopedia of Biomedical Engineering (pp. 462–482). Elsevier. https://doi.org/10.1016/B978-0-12-801238-3.64098-9

Trache, D., Tarchoun, A. F., Derradji, M., Hamidon, T. S., Masruchin, N., Brosse, N., & Hussin, M. H. (2020). Nanocellulose: From fundamentals to advanced applications. *Frontiers in Chemistry*, *8*, 392. https://doi.org/10.3389/fchem.2020.00392

Kaur, P., Sharma, N., Munagala, M., Rajkhowa, R., Aallardyce, B., Shastri, Y., & Agrawal, R. (2021). Nanocellulose: Resources, physio-chemical properties, current uses and future applications. *Frontiers in Nanotechnology*, *3*, 747329. https://doi.org/10.3389/fnano.2021.747329

Kargarzadeh, H., Huang, J., Lin, N., Ahmad, I., Mariano, M., Dufresne, A., Thomas, S., & Gałęski, A. (2018). Recent developments in nanocellulose-based biodegradable polymers, thermoplastic polymers, and porous nanocomposites. *Progress in Polymer Science*, *87*, 197–227. https://doi.org/10.1016/j.progpolymsci.2018.07.008

Yusuf, V. F., Malek, N. I., Kailasa, S. K. (2022). Review on Metal–Organic Framework Classification, Synthetic Approaches, and Influencing Factors: Applications in Energy, Drug Delivery, and Wastewater Treatment. ACS Omega, 7(49), 44507-44531. https://doi.org/10.1021/acsomega.2c05310

Furukawa, H., Cordova, K. E., O'Keeffe, M., Yaghi, O. M. (2013). The Chemistry and Applications of Metal-Organic Frameworks. Science, 341(6149), 1230444. https://doi.org/10.1126/science.1230444

Zeng, X., Hu, X., Song, H., Xia, G., Shen, Z.- Y., Yu, R., Moskovits, M. (2021). Microwave synthesis of zeolites and their related applications. Microporous and Mesoporous Materials, 323, 111262. https://doi.org/10.1016/j.micromeso.2021.111262

Elaouni, A., Ouardi, M. E., Zbair, M., BaQais, A., Saadi, M., Ahsaine, H. A. (2022). ZIF-8 metal organic framework materials as a superb platform for the removal and photocatalytic degradation of organic pollutants: A review. RSC Advances, 12(49), 31801–31817. https://doi.org/10.1039/D2RA05717D

Carey, J. P. (2017). Introduction to braided composites. In Handbook of Advances in Braided Composite Materials (pp. 1–21). Elsevier. https://doi.org/10.1016/B978-0- 08-100369-5.00001-5

Linganiso, L. Z., Anandjiwala, R. D. (2016). Fibrereinforced laminates in aerospace engineering. In Advanced Composite Materials for Aerospace Engineering (pp. 101–127). Elsevier. https://doi.org/10.1016/B978-0- 08-100037-3.00004-3

Shahbaz, M., Naeem, H., Murtaza, S., Ul-Huda, N., Tayyab, M., Hamza, A., Momal, U. (2024). Application of starch as an active ingredient for the fabrication of nanocomposite in food packaging. In Starch Based Nanomaterials for Food Packaging (pp. 161–208). Elsevier. https://doi.org/10.1016/B978-0-443-18967-8.00004-9

Di Matteo, V., Di Filippo, M. F., Ballarin, B., Gentilomi, G. A., Bonvicini, F., Panzavolta, S., & Cassani, M. C. (2023). Cellulose/zeolitic imidazolate framework (ZIF-8) composites with antibacterial properties for the management of wound infections. *Journal of Functional Biomaterials*, *14*(9), 472. https://doi.org/10.3390/jfb14090472

Molaei, R., Moradi, M., Kahyaoğlu, L. N., & Forough, M. (2022). Application of bacterial nanocellulose decorated with zeolitic imidazolate framework (Zif-l) as a platform for food freshness monitoring. *International Journal of Biological Macromolecules*, *223*, 713–721. https://doi.org/10.1016/j.ijbiomac.2022.11.051

Kida, K., Okita, M., Fujita, K., Tanaka, S., & Miyake, Y. (2013). Formation of high crystalline ZIF-8 in an aqueous solution. *CrystEngComm*, *15*(9), 1794. https://doi.org/10.1039/c2ce26847g

Chappanda, K. N., Tchalala, M. R., Shekhah, O., Surya, S. G., Eddaoudi, M., & Salama, K. N. (2018). A comparative study of interdigitated electrode and quartz crystal microbalance transduction techniques for metal–organic framework-based acetone sensors. *Sensors*, *18*(11), 3898. https://doi.org/10.3390/s18113898

Trivedi, M. K., Dahryn Trivedi, A. B., & Gunin Saikia, G. N. (2015). Physical and structural characterization of biofield treated imidazole derivatives. *Natural Products Chemistry & Research*, *03*(05). https://doi.org/10.4172/2329-6836.1000187

Malekmohammadi, M., Fatemi, S., Razavian, M., & Nouralishahi, A. (2019). A comparative study on ZIF-8 synthesis in aqueous and methanolic solutions: Effect of temperature and ligand content. *Solid State Sciences*, *91*, 108–112. https://doi.org/10.1016/j.solidstatesciences.2019.03.022

Zhang, Y., Jia, Y., Li, M., & Hou, L. (2018). Influence of the 2-methylimidazole/zinc nitrate hexahydrate molar ratio on the synthesis of zeolitic imidazolate framework-8 crystals at room temperature. *Scientific Reports*, *8*(1), 9597. https://doi.org/10.1038/s41598-018-28015-7

Yamamoto, D., Maki, T., Watanabe, S., Tanaka, H., Miyahara, M. T., & Mae, K. (2013). Synthesis and adsorption properties of ZIF-8 nanoparticles using a micromixer. *Chemical Engineering Journal*, *227*, 145–150. https://doi.org/10.1016/j.cej.2012.08.065

Allegretto, J. A., Onna, D., Bilmes, S. A., Azzaroni, O., & Rafti, M. (2024). Unified roadmap for zif-8 nucleation and growth: Machine learning analysis of synthetic variables and their impact on particle size and morphology. *Chemistry of Materials*, *36*(11), 5814–5825. https://doi.org/10.1021/acs.chemmater.4c01069

Li, J., Chang, H., Li, Y., Li, Q., Shen, K., Yi, H., & Zhang, J. (2020). Synthesis and adsorption performance of La@ZIF-8 composite metal–organic frameworks. *RSC Advances*, *10*(6), 3380–3390. https://doi.org/10.1039/C9RA10548D

Akhundzadeh Tezerjani, A., Halladj, R., & Askari, S. (2021). Different view of solvent effect on the synthesis methods of zeolitic imidazolate framework-8 to tuning the crystal structure and properties. *RSC Advances*, *11*(32), 19914–19923. https://doi.org/10.1039/D1RA02856A

Ghorbani, H., Ghahramaninezhad, M., & Niknam Shahrak, M. (2020). The effect of organic and ionic liquid solvents on structure crystallinity and crystallite size of ZIF-8 for CO2 uptake. *Journal of Solid State Chemistry*, *289*, 121512. https://doi.org/10.1016/j.jssc.2020.121512

Kumari, G., Jayaramulu, K., Maji, T. K., & Narayana, C. (2013). Temperature induced structural transformations and gas adsorption in the zeolitic imidazolate framework

zif-8: A raman study. *The Journal of Physical Chemistry A*, *117*(43), 11006–11012. https://doi.org/10.1021/jp407792a

*12 principles of green chemistry*. (n.d.). American Chemical Society. Retrieved November 2, 2024, from https://www.acs.org/greenchemistry/principles/12-principles-of-green-chemistry.html

Du, W., Wang, X., Shan, W., Wang, W., Zhang, J., & Chen, G. (2023). Synthesis, performance and inhibition mechanism of modified peanut shell nanocellulose as shale hydration inhibitor. *Polymer Bulletin*, *80*(1), 263–277. https://doi.org/10.1007/s00289-022-04097-2

Abdulhameed, Adamu & Mbuvi, Harun & Changamu, Evans & Maingi, Francis. (2019). Microwave synthesis of Carboxymethylcellulose (CMC) from Rice Husk. IOSR Journal of Applied Chemistry. 12. 33-42. 10.9790/5736-1212013342.

McArdle, W. D., Katch, F. I., & Katch, V. L. (2007). *Exercise physiology: Energy, nutrition, and human performance* (6th ed). Lippincott Williams & Wilkins.

Kazem K. (2021). Lecture 2: Pore Volume Movement. Engineering Faculty, Al Maqal University. https://almaaqal.edu.iq/wp-content/uploads/2021/12/Lecture-2_pore-volume.pdf

Pasachova Garzón, J, Ramírez Martínez, S, & Muñoz Molina, L. (2019). Staphylococcus aureus: generalidades, mecanismos de patogenicidad y colonización celular. *Nova*, *17*(32), 25-38. Retrieved November 02, 2024, from http://www.scielo.org.co/scielo.php?script=sci_arttext&pid=S1794-24702019000200025&lng=en&tlng=es.

Sirelkhatim, A., Mahmud, S., Seeni, A., Kaus, N. H. M., Ann, L. C., Bakhori, S. K. M., Hasan, H., & Mohamad, D. (2015). Review on zinc oxide nanoparticles: Antibacterial activity and toxicity mechanism. *Nano-Micro Letters*, *7*(3), 219. https://doi.org/10.1007/s40820-015-0040-x

Yang, X., Yang, D., Lin, X., Li, D., Shi, W., Xiang, Z., Mu, C., Ge, L., Li, D., & Xu, Z. (2023). Effect of dehydrothermal treatment on the structure and properties of a collagen-based heterogeneous bilayer membrane. *ACS Applied Polymer Materials*, *5*(5), 3427–3438. https://doi.org/10.1021/acsapm.3c00095